

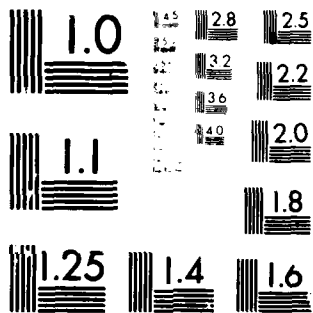
RENSSELAER POLYTECHNIC INST TROY NY DEPT OF ELECTRIC--ETC F/6 5/8
TEXTURE DISCRIMINATION BASED UPON AN ASSUMED STOCHASTIC TEXTURE--ETC(U)
MAR 80 J W MODESTINO, R W FRIES, A L VICKERS F30602-78-C-0083

RADC-TR-80-58

NL

1 of 1
 20
 (a) 100.00%

END
DATE
FILMED
6-80
DTIC



MICROCOPY RESOLUTION TEST CHART
NATIONAL BUREAU OF STANDARDS-1963-A

ADA 084047

RADC-TR-80-58
Final Technical Report
March 1980

LEVEL

12



TEXTURE DISCRIMINATION BASED UPON AN ASSUMED STOCHASTIC TEXTURE MODEL

Rensselaer Polytechnic Institute

James W. Modestino
Robert W. Fries
Acie L. Vickers

DTIC
ELECTE
MAY 9 1980
S D C

APPROVED FOR PUBLIC RELEASE; DISTRIBUTION UNLIMITED

ROME AIR DEVELOPMENT CENTER
Air Force Systems Command
Griffiss Air Force Base, New York 13441

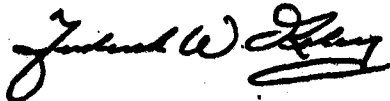
FILE COPY

80 5 8 004

This report has been reviewed by the RADC Public Affairs Office (PA) and is releasable to the National Technical Information Service (NTIS). At NTIS it will be releasable to the general public, including foreign nations.

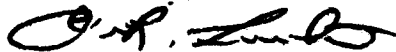
RADC-TR-80-58 has been reviewed and is approved for publication.

APPROVED:



FREDERICK W. RAHRIG
Project Engineer

APPROVED:



OWEN R. LAWTER, Colonel, USAF
Chief, Intelligence and Reconnaissance Division

FOR THE COMMANDER:



JOHN P. HUSS
Acting Chief, Plans Office

If your address has changed or if you wish to be removed from the RADC mailing list, or if the addressee is no longer employed by your organization, please notify RADC (IRRE), Griffiss AFB NY 13441. This will assist us in maintaining a current mailing list.

Do not return this copy. Retain or destroy.



MISSION of Rome Air Development Center

RADC plans and executes research, development, test and selected acquisition programs in support of Command, Control Communications and Intelligence (C³I) activities. Technical and engineering support within areas of technical competence is provided to ESD Program Offices (POs) and other ESD elements. The principal technical mission areas are communications, electromagnetic guidance and control, surveillance of ground and aerospace objects, intelligence data collection and handling, information system technology, ionospheric propagation, solid state sciences, microwave physics and electronic reliability, maintainability and compatibility.

UNCLASSIFIED

SECURITY CLASSIFICATION OF THIS PAGE (When Data Entered)

REPORT DOCUMENTATION PAGE		READ INSTRUCTIONS BEFORE COMPLETING FORM
1. REPORT NUMBER RADCL TR-80-58	2. GOVT ACCESSION NO. AD-A084 047	3. RECIPIENT'S CATALOG NUMBER
4. TITLE (and Subtitle) TEXTURE DISCRIMINATION BASED UPON AN ASSUMED STOCHASTIC TEXTURE MODEL.		5. TYPE OF REPORT & PERIOD COVERED Final Technical Report 31 Oct 1978 - 30 Oct 1979
6. AUTHOR(s) James W. Modestino Robert W. Fries Acie L. Vickers		7. PERFORMING ORG. REPORT NUMBER N/A
8. PERFORMING ORGANIZATION NAME AND ADDRESS Rensselaer Polytechnic Institute Electrical and Systems Engineering Department Troy NY 12181		9. CONTRACT OR GRANT NUMBER(s) F30602-78-C-0083
10. CONTROLLING OFFICE NAME AND ADDRESS Rome Air Development Center (IRRE) Griffiss AFB NY 13441		11. PROGRAM ELEMENT, PROJECT, TASK AREA & WORK UNIT NUMBERS 62703F 459417P1
12. MONITORING AGENCY NAME & ADDRESS (if different from Controlling Office) Same		13. REPORT DATE March 1980
14. DISTRIBUTION STATEMENT (of this Report) Approved for public release; distribution unlimited		15. NUMBER OF PAGES 65
16. DISTRIBUTION STATEMENT (of the abstract entered in Block 20, if different from Report) Same		17. SECURITY CLASS. (of this report) UNCLASSIFIED
18. SUPPLEMENTARY NOTES RADCL Project Engineer: Frederick W. Rahrig (IRRE)		19. DECLASSIFICATION DOWNGRADING SCHEDULE N/A
19. KEY WORDS (Continue on reverse side if necessary and identify by block number) Texture Discrimination Log-Likelihood Texture Discriminator Stochastic Modeling 2-D Digital Filtering Maximum Likelihood Classifier Spatial Gray-Level Co-Occurrences		
20. ABSTRACT (Continue on reverse side if necessary and identify by block number) A new approach to texture discrimination is described. This approach is based upon an assumed stochastic model for texture in imagery and is an approximation to the statistically optimum maximum likelihood classifier. The construction and properties of the stochastic texture model are described and a digital filtering implementation of the resulting maximum likelihood texture discriminant is provided. The efficacy of this approach is demonstrated through experimental results obtained with		

DD FORM 1473
1 JAN 73

EDITION OF 1 NOV 65 IS OBSOLETE

UNCLASSIFIED

SECURITY CLASSIFICATION OF THIS PAGE (When Data Entered)

UNCLASSIFIED

SECURITY CLASSIFICATION OF THIS PAGE(When Data Entered)


simulated texture data. A comparison is provided with more conventional texture discriminants under identical conditions. The implications to texture discrimination in real-world imagery are discussed.

UNCLASSIFIED

SECURITY CLASSIFICATION OF THIS PAGE(When Data Entered)

EVALUATION

This report describes an approach to texture discrimination based on spatial gray-level co-occurrences and maximum likelihood classification. This log-likelihood discriminator demonstrated its capability to discriminate between two-dimensional random fields having identical second moment properties where existing schemes based on autocorrelation and/or power spectral density and also edge density/correlation techniques could not. This effort has provided a promising contribution to accomplishing the goals of technical planning objective R2C, Digital Image Exploitation for Target Detection and Identification.


FREDERICK W. RAHRIG
Project Engineer

Accession For	
NAME ORMAI	<input checked="checked" type="checkbox"/>
DDC TAB	<input type="checkbox"/>
Unannounced	<input type="checkbox"/>
Justification	
By _____	
Distribution/	
Availability Codes	
Dist	Avail and/or special
A	

I. Introduction:

An important problem in image processing applications is the segmentation of an image field into disjoint regions which may possess the same average gray level but differ in the spatial distribution of gray levels. These two characteristics are generally referred to as tone and texture respectively, although more precise definition of these terms has remained elusive. It has been emphasized by Haralick [1], [2], among others, that a subtle relationship exists between tone and texture which depends very much upon the resolution with which an image is viewed. At both low and high resolution the dominant feature is that of tone, while at intermediate resolutions texture is often the dominant feature. The most widely accepted definition of texture at present [3]-[5] consists of a basic local order or quasi-homogeneous pattern which is repeated in a "nearly periodic" manner over some image region which is large relative to the size of the local pattern. We accept this as a working definition in what follows although with some qualification on the "nearly periodic" repetitiveness attribute.

A number of techniques for texture discrimination have been proposed and have achieved considerable success, although generally under well-defined and rather limited operating conditions. These techniques can be classified as either structural or statistical in their approach. Our interest here will be in a purely statistical approach. Structural approaches are described by Zucker [6], and Lu and Fu [7], among others. Recent work by Haralick [8] provides a comprehensive survey of most existing statistical techniques which he classifies into eight broad categories possessing some degree of overlap. For example, consider Haralick's first three categories; those based on autocorrelation functions, optical transforms, and digital transforms. In reality

these techniques are all based upon second-moment properties and can be collectively classified as such. The major classifications of statistical approaches to texture classification/discrimination are then, following Haralick, those based upon: second-moment properties, edge density, spatial similarity, spatial gray-level co-occurrence probabilities, gray-level run lengths, and finally use of two-dimensional (2-D) autoregressive modeling assumptions. As Haralick correctly points out, the spatial similarity approach is restricted to binary images while the 2-D autoregressive linear estimation approach is severely limited in the classes of texture for which it is useful. In particular, the 2-D autoregressive process does not, except under pathological assumptions, exhibit the local pattern replication attribute considered an essential ingredient of texture. As a result, the competing statistical approaches for general application to texture discrimination are reduced to the four remaining categories as enumerated above.

Many of the specific techniques in these remaining four categories are based upon heuristic or ad hoc arguments while a comparative few have been based upon the rigorous application of statistical decision theory concepts under specific stochastic modeling assumptions. A comparative study of several of the more frequently used statistical approaches is provided by Weszka, et al. [9]. In particular, the efficacy of various features, drawn from these four categories, was investigated in the context of terrain classification. While results of this nature are useful they provide little guidance on how the relative performance is affected under various modeling assumptions. It is difficult, for example, to extrapolate the results of these and similar studies to applications beyond the specific data base for which performance has been provided. Clearly, use of more general 2-D stochastic texture models

whose parameters can be easily related to texture properties would remedy this situation.

Much of the work on texture discrimination has been guided by human visual discrimination studies. Several researchers [10], [11] in this area have concluded, although with some qualification [12], that humans can effortlessly differentiate texture regions which differ in second-order statistics but cannot discriminate between regions which differ only in third and higher-order statistics. This is supported by the degree of success achieved with texture discrimination algorithms based upon second-order properties alone, such as second-moment techniques utilizing autocorrelation functions or power spectral densities. Nevertheless, for virtually all the existing techniques it is possible to contrive counterexamples which, although effortlessly discriminated by human observation, cannot be discriminated by algorithmic means.

In Fig. 1, for example, we illustrate realizations of two random fields[†] which are visually distinct yet possess identical autocorrelation functions and/or power spectral densities. These fields cannot be distinguished by algorithmic approaches based upon second-moment properties alone. Similarly, in Fig. 2, we illustrate several realizations of random fields which possess the same number of edges per unit distance and are such that the average gray-level run length along any randomly chosen line segment is identical. Again these texture regions are easily discriminated visually although algorithmic techniques based on either edge density or gray-level run lengths alone cannot discriminate the various texture regions. Finally, it is possible to contrive random fields whose joint probability density function at two points separated by a specified distance d are identical, although this need not be true for all values of d .

[†] The parameters defining the 2-D random fields in Fig.'s 1 and 2 will be described in a later section.

The implication here is that, unless the separation distance d is judiciously chosen, texture discrimination algorithms based on spatial gray-level co-occurrence probabilities are incapable of distinguishing visually distinct texture samples. Again this points out the need for texture discrimination approaches based upon rigorous application of statistical decision theory concepts under specific and flexibly parameterized stochastic modeling assumptions.

In the present paper we describe a class of 2-D random fields, of which the samples in Fig.'s 1 and 2 are selected realizations, which we feel provides a realistic and conveniently parameterized model of texture in images. This class of random fields bear some relationship to the random mosaic models for texture described by Schachter, et al. [13]. Based upon this stochastic model we propose a new approach to texture discrimination which is an approximation to the statistically optimum maximum likelihood classifier. This approach, for reasons to be described, makes use of the spatial gray-level co-occurrence matrix introduced by Haralick [1], [2]. However, unlike the Haralick approach, we do not make use of heuristically defined features for extracting texture information from the spatial gray-level co-occurrence matrix. Rather our approach is based upon a maximum likelihood hypothesis test of the gray-level co-occurrence matrix. This leads to a rather simple implementation as a 2-D digital filtering operation on the original image. Results indicate a substantial performance improvement over competing approaches.

After some preliminary comments on 2-D random fields in Section II, the construction and properties of the stochastic texture model are described in Sections III and IV respectively. The structure of the maximum likelihood texture discriminator is provided in Section V while the approximate digital implementation is described in Section VI. Typical results are illustrated in Section VII while Section VIII provides a summary and conclusions.

II. Preliminary Discussion:

We consider an image as a family of random variables $\{f_{\underline{x}}(\omega), \underline{x} \in R^2\}$, or a random field, defined on some fixed but unspecified probability space (Ω, A, P) . For convenience we suppress the functional dependence upon the underlying probability space and consistently write $f(\underline{x})$ for $f_{\underline{x}}(\omega)$. The covariance function of the random field then becomes[†]

$$R_{ff}(\underline{x}, \underline{y}) = E\{f(\underline{x})f(\underline{y})\} ; \underline{x}, \underline{y} \in R^2, \quad (1)$$

where $E\{\cdot\}$ represents the expectation operator. If a random field $\{f(\underline{x}), \underline{x} \in R^2\}$ possesses a covariance function invariant under all Euclidean motions it will be called homogeneous and isotropic (cf. [14] for definitions). In this case the covariance function of the field evaluated at two points can depend only upon the Euclidean distance between these two points so that

$$E\{f(\underline{x}+\underline{u})f(\underline{x})\} = R_{ff}(|\underline{u}|), \quad (2)$$

where $\underline{u}^T = (u_1, u_2)$ is an element of R^2 and $|\underline{u}|$ represents the ordinary Euclidean norm defined in terms of an inner product $\langle \cdot, \cdot \rangle$ according to

$$|\underline{u}|^2 = \langle \underline{u}, \underline{u} \rangle = u_1^2 + u_2^2. \quad (3)$$

By construction, the 2-D random fields to be described here are of this category. Furthermore, they have been explicitly constructed so that the joint probability density function (p.d.f.) of the field evaluated at two points likewise depends only upon the Euclidean distance between these points. More specifically, define the random variables $f_1 = f(\underline{x})$ and $f_2 = f(\underline{x}+\underline{u})$. The joint p.d.f. associated with these two random variables, parameterized by the spatial coordinates, then satisfies

$$p\{f_1, f_2; \underline{x}, \underline{x}+\underline{u}\} = p\{f_1, f_2; |\underline{u}|\}, \quad (4)$$

[†] We assume the field is of second order (i.e., variances exist) and possesses zero mean.

which is the 2-D concept of stationarity [15] or invariance which will be most useful for our purposes.

The corresponding power spectral density function is given by

$$S_{ff}(\underline{\omega}) = \int_{R^2} R_{ff}(|\underline{u}|) \exp\{-j \langle \underline{\omega}, \underline{u} \rangle\} d\underline{u} , \quad (5)$$

where $\underline{\omega}^T = (\omega_1, \omega_2)$ represents a 2-D spatial frequency vector and $d\underline{u}$ is the differential volume element in R^2 . This expression can be evaluated up to functional form with the aid of a theorem of Bochner [16] with the result

$$S_{ff}(\underline{\omega}) = S(\Omega) = 2\pi \int_0^\infty \lambda R_{ff}(\lambda) J_0(\lambda \Omega) d\lambda , \quad (6)$$

where $\Omega \triangleq |\underline{\omega}| = (\omega_1^2 + \omega_2^2)^{1/2}$ represents radial frequency. Here $J_0(\cdot)$ denotes the ordinary Bessel function of the first kind of order zero. The quantities $S_{ff}(\cdot)$ and $R_{ff}(\cdot)$ are then related through a Hankel transform [17], [18].

An important aspect of the approach to texture discrimination described here is the use of a stochastic texture model whose second-order statistics are invariant under both translation and rotation. Various stochastic texture models proposed previously do not possess this property. For example, much use has been made of 2-D autoregressive models [19]-[21] for texture, often under a separability assumption in the two orthogonal spatial directions. These processes cannot possess second-order statistics invariant under all rigid body motions. On the other hand, we feel strongly that a reasonable texture model should possess this property. Texture should retain its identity regardless of the orientation or perspective in which it is presented. Use of naturally occurring textures exhibiting obvious directional properties, such as those in the book by Brodatz [22], serves only to obscure this issue.

Had many of these samples been presented in a different orientation would a different texture category have resulted? We feel rather that these examples should be more properly considered sample fields or realizations of a random field as defined here. While particular realizations may well exhibit directional characteristics, the ensemble properties, at least up to second-order statistics, should be invariant under rigid body motions.

Another criticism of existing stochastic texture models, such as autoregressive processes, is the inability to account for the predominant and pronounced edge structure present in real-world imagery. Often this edge structure provides an important aspect of the rather imprecise concept of perceived texture. Finally, and most importantly, existing stochastic texture models do not provide the basic repetition of a local order or pattern generally considered [3], [4] an important ingredient of texture. The stochastic texture models described in the next section remove many of these objections. Furthermore, the mathematical tractability associated with these models allows straightforward development of statistically optimum texture discrimination algorithms.

III Construction of Random Field Models of Texture:

The class of random fields to be used as stochastic texture models can be described as marked point processes [23] evolving according to a spatial parameter. According to this model the plane is randomly partitioned into a number of disjoint geometric regions by an appropriately defined field of random lines which form the boundaries of these regions. The density of these random lines, or edges, is defined in terms of a rate parameter λ . Gray levels are then assigned within elementary regions to possess correlation coefficient ρ with gray levels in contiguous regions. We describe

several schemes for partitioning the plane into elementary geometrical regions. Given a particular partitioning scheme, the random fields are completely defined in terms of the two parameters λ and ρ . The parameter λ represents the "edge business" associated with an image while ρ is indicative, at least on an ensemble basis, of the "edge contrast". For ρ large (in magnitude) and negative there is an abrupt almost black-to-white or white-to-black transition across an edge boundary. If $\rho > 0$, on the other hand, the transition across an edge boundary is much more gradual. It is relatively easy to define these parameters for wide classes of imagery data.

In the present section we describe the construction of this class of 2-D random fields. Relevant second-order properties are discussed in the next section. We begin with the case where the plane is partitioned into random rectangular regions.

Rectangular Partitions: A fundamental role in the construction of this class of processes will be played by the integer-valued random field[†] $\{N(\underline{x}), \underline{x} \geq 0\}$ which provides a 2-D generalization of a counting process [24]. In particular, suppose the vector $\tilde{\underline{x}}$ is obtained from \underline{x} according to $\tilde{\underline{x}} = \underline{A} \underline{x}$ where \underline{A} is the unitary matrix

$$\underline{A} = \begin{bmatrix} \cos\theta & \sin\theta \\ -\sin\theta & \cos\theta \end{bmatrix}, \quad (7)$$

defined for some $\theta \in [-\pi, \pi]$. This transformation results in a rotation of the Cartesian coordinate axes (x_1, x_2) by θ radians as illustrated in Fig. 3.

Consider now the integer-valued random field defined by

$$N(\underline{x}) = N_1(\tilde{x}_1) + N_2(\tilde{x}_2); \quad \underline{x} \geq 0, \quad (8)$$

[†] By the notation $\underline{x} \geq 0$ we mean that $\underline{x}^T = (x_1, x_2)$ is such that $x_i \geq 0$, $i=1,2$

where $\theta \in [-\pi, \pi]$ is chosen according to some p.d.f. $p(\theta)$ and $\{N_i(\ell), \ell \geq 0\}$, $i=1,2$, are mutually independent 1-D counting processes. That is, $N_i(\ell)$ represents the number of events which have occurred in the interval $[0, \ell]$. We will be particularly concerned with the case where $\{N_i(\ell), \ell \geq 0\}$, $i=1,2$, are renewal point processes defined in terms of their interarrival distribution.

The random field $\{N(\underline{x}), \underline{x} \geq 0\}$ in (8) then assumes constant integer values on non-overlapping rectangles whose sides are parallel to the transformed axes (\hat{x}_1, \hat{x}_2) and whose locations are determined by the event times of the corresponding point processes $\{N_i(\ell), \ell \geq 0\}$, $i=1,2$. Consider now the random field $\{f(\underline{x}), \underline{x} \geq 0\}$ which undergoes transitions at the boundaries of these elementary rectangles. The gray level assumed throughout any elementary rectangle is zero-mean Gaussian[†] with variance σ^2 and correlation coefficient ρ with the gray levels in contiguous rectangles. More specifically, let $X_{i,j}$ represent the amplitude or gray level assumed by the random field after i transitions in the \hat{x}_1 direction and j transitions in the \hat{x}_2 direction. The sequence $\{X_{i,j}\}$ is assumed generated recursively according to

$$X_{i,j} = \rho X_{i-1,j} + \rho X_{i,j-1} - \rho^2 X_{i-1,j-1} + W_{i,j} \quad ; i,j \geq 1, \quad (9)$$

where $|\rho| \leq 1$, and $\{W_{i,j}\}$ is a 2-D sequence of independent and identically distributed (i.i.d.) zero-mean Gaussian variates with common variance $\sigma_w^2 = \sigma^2(1-\rho^2)^2$. The initial values $X_{k,0}, X_{0,\ell}$, $k, \ell \geq 0$ are jointly distributed zero-mean Gaussian variates with common variance σ^2 and covariance properties chosen to result in stationary conditions. An alternative interpretation of the sequence $\{X_{i,j}\}$ is as the output of a separable 2-D recursive filter excited by a white noise field. It is easily seen that

[†] For definiteness we assume Gaussian statistics. This assumption is not critical to the development which follows and is easily removed.

$$E\{X_{i,j}X_{i+k_1,j+k_2}\} = \sigma^2 \rho^{k_1+k_2} ; k_1, k_2 \geq 0 \quad (10)$$

Typical computer-generated realizations of the resulting random field are illustrated in Fig. 4 for selected values of ρ when $p(\theta)$ is uniform over $[-\pi, \pi]$ and $\{N_i(\ell), \ell \geq 0\}$, $i=1,2$, are Poisson with intensities $\lambda_1 = \lambda_2 = \lambda$. The displayed images here and throughout this paper are square arrays consisting of 256 elements or samples on a side. In Fig. 4, λ is measured in normalized units of events per sample distance so that there are on average 256λ transitions along each of the orthogonal axes. Similarly in Fig. 5 we illustrate realizations of the resulting random field when the point processes $\{N_i(\ell), \ell \geq 0\}$, $i=1,2$, undergo jumps of unit height at equally spaced intervals $\ell=1/\lambda$. The starting positions ϵ_i , $i=1,2$, will be assumed uniformly distributed over the interval $[0, \ell]$.

The preceding two examples are special cases of the situation where the point processes $\{N_i(\ell), \ell \geq 0\}$, $i=1,2$, are stationary renewal processes [25], [26] with Gamma distributed interarrival times. This class of random fields represents a 2-D generalization of the class of 1-D processes described in [27]. In particular, we assume the common interarrival distribution of the two mutually independent point processes $\{N_i(\ell), \ell \geq 0\}$, $i=1,2$, possesses p.d.f.

$$f(x) = \frac{x^{\nu-1}}{\Gamma(\nu)\beta^\nu} \exp\{-x/\beta\} , \quad (11)$$

where $\nu=1,2,\dots$, and $\beta=1/\lambda\nu$ for fixed $\lambda>0$. For example, if $\nu=1$ we have the exponential distribution

$$f(x) = \lambda e^{-\lambda x} ; x \geq 0 , \quad (12)$$

associated with the Poisson process, while in the limit $\nu \rightarrow \infty$ we have

$$f(x) = \delta(x-1/\lambda) ; x \geq 0 , \quad (13)$$

corresponding to the case of periodic partitions as illustrated in Fig. 5.

In Fig. 6 we illustrate selected realizations of the resulting random field for several values of v all with $\lambda=0.05$ and $\rho=0.0$. Clearly the parameter v provides a measure of the degree of randomness or "homogeneity" of the structure. In this sense, this model does provide the pattern replication attribute. For small v the random field $\{f(\underline{x}), \underline{x} \in R^2\}$ appears as a random rectangular mosaic. As v increases, individual realizations rapidly approach a more periodic mosaic in appearance. The parameters λ , ρ and v then completely describe this class of 2-D random fields.

Although this class of 2-D random fields provides a useful model of texture in selected applications, the rectangular mosaic exhibited by individual realizations is not entirely consistent with edge structure in real-world imagery. That is, we would expect the edge structure to exhibit a much more random edge orientation. An alternative approach then is to randomly partition the plane into more complex geometric regions. In what follows we describe one such approach where the plane is partitioned into random polygonal regions. Other approaches are described in [28], [29].

Polygonal Partitions: Consider the partition of the plane R^2 by a field of random sensed lines. More specifically, an arbitrary sensed line can be described in terms of the 3-tuple (r, θ, ζ) . Here r represents the perpendicular or radial distance to the line in question, $\theta \in [-\pi, \pi]$ represents the orientation of this radial vector, and finally ζ is a binary random variable assuming values ± 1 which specifies the sense or direction imparted to this line segment. The pertinent geometry is illustrated in Fig. 7 for the case $\zeta=1$. By virtue of the direction imposed on this line segment the plane is partitioned into two disjoint regions, R (right of line) and L (left of line) such that $R \cup L = R^2$.

Now consider the field of lines generated by the sequence $\{r_i, \theta_i, \zeta_i\}$. Here the sequence $\{r_i\}$ represents the "event times" associated with a

homogeneous Poisson process $\{N(r), r \geq 0\}$ with intensity λ events/unit distance evolving according to the radial parameter r . The sequence $\{\theta_i\}$ is i.i.d. and uniform on $[-\pi, \pi]$ while $\{\zeta_i\}$ is also i.i.d. assuming the values ± 1 with equal probability.

The field of random lines so generated results in a partition of the plane into disjoint polygonal regions. Gray levels are assigned as described in [30] to result in correlation coefficient ρ with gray levels in contiguous regions. Typical realizations of the resulting random field are illustrated in Fig. 8 for selected values of $\lambda_e = \lambda/\pi$ and ρ . The quantity λ_e represents the average edge density along any randomly chosen line segment.[†] This random field is again described in terms of the two parameters λ_e , or equivalently λ , and ρ . This class of 2-D random fields can be extended to include more general point processes $\{N(r), r \geq 0\}$ controlling the radial evolution; for example, stationary renewal processes with Gamma distributed interarrival times. Unfortunately, the analysis of the resulting processes becomes quite complicated and as a result we will not pursue this generalization here.

IV. Second-Order Properties

We turn now to the second-order properties of the class of 2-D random fields described in the preceding section. In the interests of brevity the treatment will be condensed and will make extensive use of results reported elsewhere.

Rectangular Partitions: As a first step in the development of the covariance function, assume that the random orientation $\theta \in [-\pi, \pi]$ has been chosen and that k transitions have occurred^{††} between the two points \underline{x} and $\underline{x} + \underline{u}$ where we assume for the moment $\underline{u} \geq 0$. It follows from (10) that

[†] Similarly, in the case of rectangular partitions it is easily shown that the average edge density along any randomly chosen line segment is $\lambda_e = 4\lambda/\pi$. We will consistently use the subscript e to indicate edge density along a randomly chosen line segment to distinguish from the corresponding unsubscripted rate parameter λ generating the random partition.

^{††} By this we mean that $k = k_1 + k_2$ where $k_i, i=1,2$, represents the number of transitions along each of the orthogonal axes which have now been rotated by θ radians.

$$E\{f(\underline{x}+\underline{u})f(\underline{x})|\theta, k\} = \sigma^2 \rho^k ; \quad k=0,1,2,\dots \quad (14)$$

The conditioning upon k is easily removed according to

$$E\{f(\underline{x}+\underline{u})f(\underline{x})|\theta\} = \sum_{k=0}^{\infty} E\{f(\underline{x}+\underline{u})f(\underline{x})|\theta, k\} p_{k|\theta}(\underline{u}) , \quad (15)$$

where $p_{k|\theta}(\underline{u})$ is the probability of k transitions between \underline{x} and $\underline{x}+\underline{u}$ given that θ is acting. We exploit the stationary renewal properties of the point processes $\{N_i(\ell), \ell \geq 0\}$, $i=1,2$, in writing this probability as a function only of the displacement \underline{u} . In particular, $p_{k|\theta}(\underline{u})$ can be evaluated according to

$$p_{k|\theta}(\underline{u}) = \sum_{j=0}^k q_{k-j|\theta}^{(1)}(\tilde{u}_1) q_{j|\theta}^{(2)}(\tilde{u}_2) ; \quad k=0,1,\dots , \quad (16)$$

where $q_{j|\theta}^{(i)}(\tilde{u}_i)$ is the probability that $\{N_i(\ell), \ell \geq 0\}$ has undergone j transitions in the interval \tilde{u}_i , $i=1,2$, which depends upon $\underline{u}^T = (u_1, u_2)$ and θ according to

$$\tilde{u}_1 = u_1 \cos \theta + u_2 \sin \theta, \quad (17a)$$

and

$$\tilde{u}_2 = u_2 \cos \theta - u_1 \sin \theta. \quad (17b)$$

Substituting (14) and (16) into (15) we obtain

$$E\{f(\underline{x}+\underline{u})f(\underline{x})|\theta\} = \sigma^2 \sum_{k=0}^{\infty} \rho^k \sum_{j=0}^k q_{k-j|\theta}^{(1)}(\tilde{u}_1) q_{j|\theta}^{(2)}(\tilde{u}_2) , \quad (18)$$

and by simple rearrangement of the double summation in this last expression we find

$$\begin{aligned} E\{f(\underline{x}+\underline{u})f(\underline{x})|\theta\} &= \sigma^2 \sum_{j=0}^{\infty} \sum_{k=j}^{\infty} \rho^{k-j} q_{k-j|\theta}^{(1)}(\tilde{u}_1) \rho^j q_{j|\theta}^{(2)}(\tilde{u}_2) \\ &= \sigma^2 \left[\sum_{m=0}^{\infty} \rho^m q_{m|\theta}^{(1)}(\tilde{u}_1) \right] \cdot \left[\sum_{n=0}^{\infty} \rho^n q_{n|\theta}^{(2)}(\tilde{u}_2) \right] . \end{aligned} \quad (19)$$

Assuming a uniform distribution for θ , it follows that the covariance function becomes

$$R_{ff}(\underline{x}+\underline{u}, \underline{x}) = \frac{1}{2\pi} \int_{-\pi}^{\pi} E\{f(\underline{x}+\underline{u})f(\underline{x})|\theta\} d\theta , \quad (20)$$

with the integrand given by (19). While not immediately apparent, it is easily shown that this last expression depends only upon $||\underline{u}||$ so that the resulting random field is indeed homogeneous and isotropic.

While explicit evaluation of (20) is in general quite cumbersome, it can be evaluated in special cases. For example, in the Poisson case $\nu=1$, it can be shown [31] that

$$R_{ff}(|\underline{u}|) = \frac{2\sigma^2}{\pi} \int_0^{\pi/2} \exp\{-\sqrt{2}(1-\rho)\lambda||\underline{u}||\cos(\theta-\pi/4)\}d\theta \quad (21)$$

while the corresponding power spectral density computed according to (6) becomes

$$S_{ff}(\Omega) = \frac{8(1-\rho)\lambda\sigma^2}{\Omega^2+2(1-\rho)^2\lambda^2} \left[\frac{1}{\Omega^2+(1-\rho)^2\lambda^2} \right]^{1/2} \quad (22)$$

Typical covariance surfaces together with intensity plots of the corresponding power spectral density in the case of periodic partitions (i.e., $\nu=\infty$) are illustrated in Fig. 9. The autocorrelation functions are plotted as a function of the normalized spatial variable[†] $||\underline{u}||/\ell$ over the range $0 \leq ||\underline{u}||/\ell \leq 3$, while the power spectral density is plotted as a function of the normalized spatial frequency variable $\Omega/2\pi\lambda$ over the range $0 \leq \Omega/2\pi\lambda \leq 5$. Additional details can be found in [32]. Explicit evaluation of these quantities for the general case of Gamma distributed interarrival times is provided in [29].

Similarly, the conditional joint probability of $f_1=f(\underline{x})$ and $f_2=f(\underline{x}+\underline{u})$ given both the random angle θ and the number of transitions k between \underline{x} and $\underline{x}+\underline{u}$ is easily shown to be given by^{††}

$$\begin{aligned} p\{f_1, f_2; \underline{x}, \underline{x}+\underline{u} | \theta, k\} &= \frac{1}{2\pi\sigma^2\sqrt{1-\rho^{2k}}} \exp\left\{-\frac{f_1^2-2\rho^k f_1 f_2+f_2^2}{2\sigma^2(1-\rho^{2k})}\right\}; \quad k>0 \\ &= \frac{1}{\sqrt{2\pi}\sigma} \exp\left\{-\frac{f_1^2}{2\sigma^2}\right\} \delta(f_1-f_2) \quad ; \quad k=0 \quad (23) \end{aligned}$$

[†]Here $\ell = 1/\lambda$ with λ the common rate parameter of the two mutually independent point processes which provide rectangular partition of the plane.

^{††}It is at this point that the Gaussian assumption is crucial.

Note that this quantity is independent of \underline{x} , $\underline{x}+\underline{u}$ and θ ; we will make use of this observation later.

The conditioning upon k in this case is easily removed according to

$$\begin{aligned} p\{f_1, f_2; \underline{x}, \underline{x}+\underline{u}|\theta\} &= \sum_{k=0}^{\infty} p\{f_1, f_2; \underline{x}, \underline{x}+\underline{u}|\theta, k\} p_{k|\theta}(\underline{u}) \\ &= \sum_{k=0}^{\infty} h_k(f_1, f_2) p_{k|\theta}(\underline{u}) \quad , \end{aligned} \quad (24)$$

where $p_{k|\theta}(\underline{u})$ has been defined previously as the probability of k transitions between \underline{x} and $\underline{x}+\underline{u}$ given that θ is acting. We have used $h_k(f_1, f_2)$ in the second expression of (24) in order to emphasize the functional independence of the spatial parameters \underline{x} and $\underline{x}+\underline{u}$ and the rotation angle θ .

Again under the assumption of uniform distribution for θ , the joint p.d.f. can be evaluated as

$$p\{f_1, f_2; \underline{x}, \underline{x}+\underline{u}\} = \frac{1}{2\pi} \int_{-\pi}^{\pi} p\{f_1, f_2; \underline{x}, \underline{x}+\underline{u}|\theta\} d\theta = \sum_{k=0}^{\infty} h_k(f_1, f_2) p_k(|\underline{u}|), \quad (25)$$

where

$$p_k(|\underline{u}|) \triangleq \frac{1}{2\pi} \int_{-\pi}^{\pi} p_{k|\theta}(\underline{u}) d\theta \quad , \quad (26)$$

and we have made explicit use of the fact that the integral on the right-hand side of this last expression depends only upon the Euclidean distance $|\underline{u}|$. It follows that (4) is indeed satisfied and hence the 2-D random field is homogeneous and isotropic through all second-order statistics.

To complete the evaluation of the joint p.d.f. $p\{f_1, f_2; |\underline{u}|\}$ it remains to provide explicit evaluation of $p_k(|\underline{u}|)$ in (26). This has proven quite cumbersome in general, although quite tractable in several important special cases. For example, again in the case $v=1$ corresponding to Poisson partitions, it can be shown [29] that

$$p_k(|\underline{u}|) = \frac{4[\sqrt{2}\lambda|\underline{u}|]^k}{\pi k!} \int_0^{\pi/4} \cos^k \theta \exp\{-\sqrt{2}\lambda|\underline{u}|\cos\theta\} d\theta; \quad k=0,1,\dots, \quad (27)$$

which does not seem capable of further simplification. At any rate, this expression is easily evaluated by numerical integration. Substitution into (25) then yields explicit evaluation of $p\{f_1, f_2; |\underline{u}|\}$. Actually, for evaluation and display purposes, it proves convenient to consider a normalized version of this joint p.d.f. defined according to[†]

$$p_0\{f_1, f_2; |\underline{u}|\} = \sigma^2 p\{\sigma f_1, \sigma f_2; |\underline{u}|\}, \quad (28)$$

which is plotted in Fig. 10 as a function of f_1, f_2 for selected values of ρ and the normalized displacement $d' \triangleq \lambda_e |\underline{u}|$. Here the point $f_1 = f_2 = 0$ appears in the center and the plots cover the range $-3 \leq f_i \leq 3$, $i=1,2$. Note the high concentration of discrete probability mass along the diagonal $f_1 = f_2$ for small values of d' . This is a direct result of the high probability of \underline{x} and $\underline{x} + \underline{u}$ falling in the same rectangular regions and thus resulting in identical values for $f_1 = f(\underline{x})$ and $f_2 = f(\underline{x} + \underline{u})$. This probability diminishes for increasing d' . Indeed, as indicated in Fig. 10, this "ridge line" along the diagonal has virtually disappeared for $d' = 8$. The off-diagonal probability mass visible for $\rho = -0.9$ is a direct result of the negative correlation while for $\rho = 0.5$, as expected, there is visible probability mass distributed along the main diagonal. For $\rho = 0$, of course, this distribution is circularly symmetric about the origin. These observations are more apparent in Fig. 11 which illustrates intensity plots of the logarithms of the corresponding p.d.f.'s in Fig. 10. Note, the almost identical circularly symmetric distributions which result for large d' independent of the value of ρ . This says, in particular, that if random fields possessing different values of ρ are to be distinguished on the basis

[†] The net effect of this normalization is that the f_1, f_2 axes can be considered normalized to the standard deviation σ .

of second-order probability distributions the normalized displacement d' must be chosen judiciously. Values of d' which are either too small or too large provide little discrimination ability. Values of d' close to unity appear to offer the maximum discrimination ability. We will have more to say on this point later.

Polygonal Partitions: The second-order properties of this 2-D random field have been described in some detail in [30]. Here it is shown that, under the assumption of a Poisson line process generating the partitions, the autocorrelation function is given by

$$R_{ff}(|\underline{u}|) = \sigma^2 e^{-\lambda_e |\underline{u}|} \{ I_0(\lambda_e |\underline{u}|) + 2 \sum_{k=1}^{\infty} \rho^k I_k(\lambda_e |\underline{u}|) \}, \quad (29)$$

where $I_k(\cdot)$ is the modified Bessel function of the first kind of order k .

Similarly, the corresponding power spectral density is evaluated according to

$$S_{ff}(\Omega) = \frac{2\sigma^2(1-\rho^2)}{\lambda_e^2} \int_0^\pi \left[\frac{1-\cos\phi}{1-2\rho\cos\phi+\rho^2} \right] \frac{d\phi}{[(\Omega/\lambda_e)^2 + (1-\cos\phi)^2]^{3/2}}. \quad (30)$$

These quantities are illustrated in Fig. 12 for various values of ρ . One notable characteristic of this random field is that the power spectral density behaves as $(\Omega/\lambda_e)^{-3/2}$ for small values of (Ω/λ_e) , i.e., $S_{ff}(\Omega)$ has a singularity at the origin except for $\rho=-1$. This high concentration of energy at low spatial frequencies is a direct result of the construction procedure which allows relatively large correlations between gray levels in regions relatively far apart. We feel that this characteristic is typical of selected texture processes and as a result it was purposely built into the construction procedure.

Finally, following the procedure described previously in the case of rectangular partitions, the joint p.d.f. is easily shown to be given by (25) with the sum extended over both positive and negative values of k and

$$p_k(|\underline{u}|) = [\lambda_e |\underline{u}|/2]^{|k|} \exp\{-\lambda_e |\underline{u}|\} \sum_{l=0}^{\infty} \frac{[\lambda_e |\underline{u}|/2]^{2l}}{(l+|k|)! l!} ; \quad k=0, \pm 1, \pm 2, \dots (30)$$

In Fig. 13 we provide intensity plots of the logarithm of $p_0\{f_1, f_2; |\underline{u}|\}$ as a function of f_1 and f_2 for selected values of ρ and $d' = \lambda_e |\underline{u}|$. An interesting observation to be drawn here is the persistence of the diagonal "ridge line" with increasing values of d' . This is, of course, a direct result of the construction procedure which allows return to the same gray level at distant spatial locations with relatively high probability.

Comment: The comments made previously in relationship to Fig.'s 1 and 2 can now be explained in terms of the preceding properties of the 2-D random field models of texture. For example, in the case of rectangular Poisson partitions the autocorrelation function and/or power spectral density, computed according to (21) and (22) respectively, depend only upon the product $(1-\rho)\lambda$. The sample fields in Fig. 1 have been chosen to maintain a constant value for this product and hence possess identical second-moment properties. Similarly, for this random field the average edge density along any randomly chosen line segment can be shown to be given by $\lambda_e = 4\lambda/\pi$. The sample random fields in Fig. 2 all possess identical values for λ_e and hence cannot be distinguished on the basis of either edge density or average gray-level run lengths alone. Finally, as we have observed in conjunction with Fig.'s 10 and 11, it is possible for two visually distinct random fields to possess the same joint p.d.f. for some, but clearly not all, displacement distances d' . Again this points out a potential problem associated with discrimination approaches based upon spatial gray-level co-occurrence probabilities.

V. Log-Likelihood Texture Discriminator:

We suppose that each point of an image array $\{f_{i,j}\}_{i,j=1}^N$ is known to be associated with one of a finite number K of texture classes or hypotheses labeled H_i , $i=0,1,\dots,K-1$, respectively. Furthermore, the array $\{f_{i,j}\}_{i,j=1}^N$ will be assumed to have been obtained by discrete homogeneous sampling of corresponding sample functions $\{f(\underline{x}), \underline{x} \in \mathbb{R}^2\}$ of 2-D random fields as described in preceding sections. Typical realizations are illustrated in Fig. 14 in the case of the rectangular partition process. Here various texture samples are provided in different corners of an image which are labeled as points on a compass, i.e., NW indicates the northwest corner, E indicates the east, etc. In the top row of Fig. 14, the parameter v is held fixed for each image while ρ is varied. Similarly, in the bottom row ρ is held fixed for each image while v is varied. In all cases the edge density is held fixed at $\lambda=0.50$. Additional examples have been provided previously in Fig.'s 1 and 2. Our interest then will be in discriminating between the various texture regions and accurately detecting the boundaries between these regions.

An optimum texture discriminator, which minimizes the classification error, should clearly be based on a threshold test on the likelihood functional or some monotonic function of it [33], [34]. More specifically, suppose a window of size $(2M+1) \times (2M+1)$ is constructed about each pixel position (i,j) . The observations at pixel positions within the window centered at position (i,j) will be denoted

$$F_{i,j} = \{f_{k,l}; i-M \leq k \leq i+M, j-M \leq l \leq j+M\}; \quad i,j=1,2,\dots,N, \quad (32)$$

where we assume $M < N$ and neglect the boundary effects. The likelihood functional with the window centered on pixel position (i,j) and assuming the

k'th hypothesis acting is then defined according to

$$\Lambda_k\{F_{i,j}\} \triangleq \frac{p\{F_{i,j}|H_k\}}{p_0\{F_{i,j}\}} \quad ; \quad k=0,1,\dots,K-1 \quad , \quad (33)$$

where $p_0\{\cdot\}$ is an appropriately defined p.d.f. independent of which hypothesis is acting and serving merely to provide a convenient normalization. As the window is scanned accross the image array $\{f_{i,j}\}_{i,j=1}^N$, each pixel position is assigned the value $k(i,j)$ corresponding to the index which maximizes the class-conditional likelihood functional in (33). That is, $k(i,j) = k_0$ if

$$\Lambda_{k_0}\{F_{i,j}\} = \max_{0 \leq k \leq K-1} \Lambda_k\{F_{i,j}\} \quad . \quad (34)$$

In this way each point will be assigned to one of a predetermined collection of texture classes on the basis of local gray level values in a way that minimizes the classification error. Boundaries can be determined by edge detection of the resulting array $\{k(i,j)\}_{i,j=1}^N$.

There are several difficulties with the approach described above. First, in order to implement the likelihood functional in (33) we require explicit knowledge of the joint p.d.f. of order $(2M+1) \times (2M+1)$ for the underlying 2-D random field $\{f(\underline{x}), \underline{x} \in R^2\}$. It is very rare that this information would be available. For the 2-D random fields described in the preceding sections we have been able to determine the joint p.d.f. $p\{f_1, f_2; ||\underline{u}||\}$ for two points separated by the distance $||\underline{u}||$; higher order p.d.f.'s are somewhat intractable. Furthermore, even if these high-order p.d.f.'s were available any texture discrimination approach based upon the likelihood functional would be so finely tuned to the modeling assumptions that it may be of questionable utility in a practical application. We might prefer a suboptimum although, hopefully, more robust approach.

A reasonable suboptimum approach would be to perform a data reduction on the sequence $\{F_{i,j}\}$ of observations to result in measurements which are more tractable and at the same time relatively robust. The reduced data can then be used in a subsequent log-likelihood discriminator. There are many candidates for the data reduction operation. We have found it useful to make use of histograms of gray-level co-occurrences. More specifically, suppose that the original image array $\{f_{i,j}\}_{i,j=1}^N$ is quantized to Q levels labeled $0, 1, \dots, Q-1$. Haralick and his co-workers [1]-[2] have introduced the concept of the gray-level co-occurrence matrix. This is a $Q \times Q$ matrix with (m,n) element $p_{i,j}(m,n; d, \theta)$ defined as the number of times the gray levels m and n occur separated by d pixels at an angle θ within a window of size $(2M+1) \times (2M+1)$ centered at pixel position (i,j) . Furthermore, since the texture models under consideration are invariant under rotations we utilize a version of the co-occurrence matrix which is an average over all θ and denote the result by $P_{i,j}(d)$. The proposed texture discriminator is then implemented as a log-likelihood test on the sequence $\{P_{i,j}(d)\}$ for a fixed value of d . A block diagram of the resulting log-likelihood discriminator is illustrated in Fig. 15. The pixel position (i,j) is assigned the value $k(i,j)=k_0$ if

$$L_{k_0}\{P_{i,j}(d)\} = \max_{0 \leq k \leq K-1} L_k\{P_{i,j}(d)\} , \quad (35)$$

where

$$L_k\{P_{i,j}(d)\} \triangleq \ln \frac{p\{P_{i,j}(d)|H_k\}}{p_0\{P_{i,j}(d)\}} ; \quad k=0,1,\dots,K-1 , \quad (36)$$

represents the class-conditional log-likelihood functional.

Haralick has advocated use of the gray-level co-occurrence matrix differently than that described here. More specifically, he has proposed

14 functionals or discriminants defined on the gray-level co-occurrence matrix which are intended to discriminate among different texture regions. While these quantities have been shown to be of value in selected applications they are based upon heuristics for the most part. Here the use of $P_{i,j}(d)$ in a maximum likelihood detector is more solidly based on statistical decision theory concepts. The primary motivation for employing $P_{i,j}(d)$ to effect the data reduction in Fig. 15 is the analytical simplicity which results. The conditional p.d.f.'s $p\{P_{i,j}(d)|H_k\}$, $k=0,1,\dots,K-1$ are easily evaluated in terms of the joint p.d.f. $p\{f_1, f_2; |\underline{u}|\}$ as demonstrated below. Use of second-order p.d.f.'s provides a logical extension of techniques based upon either correlation properties or edge density. This choice has also been influenced by the general inability of humans to discriminate textures which differ only in higher order statistics.

In the implementation of the log-likelihood texture discriminator a critical simplifying assumption is made concerning the construction of the $P_{i,j}(d)$ matrix. Specifically, we assume that each pair of points counted in producing $P_{i,j}(d)$ has its intensities assigned independently of every other pair of points. Clearly this is not generally the case for the 2-D random fields described in preceding sections. Nevertheless, justification to some extent follows from the assumed ergodic properties of the underlying random fields. In particular, we assume that spatial averages over the observation window approach ensemble averages asymptotically as the size of the window increases. As a result, the empirical distributions constituting elements of $P_{i,j}(d)$ approximate the true probability distributions of corresponding spatial gray-level co-occurrence events. Hence, provided the observation window is large enough, the matrix $P_{i,j}(d)$ is indistinguishable from that which would have been obtained from a set of independent samples of the same process.

The description of the log-likelihood texture discriminator illustrated in Fig. 15 is then complete once explicit evaluation of the class-conditional log-likelihood functionals $L_k\{P_{i,j}(d)\}$ is provided. Under the independence assumption described above, the evaluation of $p\{P_{i,j}(d)|H_k\}$, $k=0,1,\dots,K-1$, is described in terms of the multinomial distribution [15],

$$p\{P_{i,j}(d)|H_k\} = \frac{\left(\sum_{m,n=0}^{Q-1} p_{i,j}(m,n;d)\right)!}{\prod_{m,n=0}^{Q-1} (p_{i,j}(m,n;d))!} \frac{Q-1}{\prod_{m,n=0}^{Q-1} Q_{m,n}(d;H_k)} \left[Q_{m,n}(d;H_k)\right]^{p_{i,j}(m,n;d)}, \quad (37)$$

where $Q_{m,n}(d;H_k)$ is the probability of observing gray levels m and n at a particular pair of points separated by distance d under hypothesis H_k , $k=0,1,\dots,K-1$. For convenience we take the normalization functional[†] $p_0\{P_{i,j}(d)\}$ as

$$p_0\{P_{i,j}(d)\} = \frac{\left(\sum_{m,n=0}^{Q-1} p_{i,j}(m,n;d)\right)!}{\prod_{m,n=0}^{Q-1} (p_{i,j}(m,n;d))!} \quad (38)$$

It follows from (36) that the class-conditional log-likelihood functionals are given by

$$L_k\{P_{i,j}(d)\} = \sum_{m=0}^{Q-1} \sum_{n=0}^{Q-1} p_{i,j}(m,n;d) \ell_k(m,n;d); \quad k=0,1,\dots,K-1, \quad (39)$$

where

$$\ell_k(m,n;d) \triangleq \ln Q_{m,n}(d;H_k). \quad (40)$$

This latter quantity is easily computed from the joint p.d.f. of the underlying 2-D random field. Suppose that the $\{f_k(\underline{x}), \underline{x} \in R^2\}$ represents the random field associated with hypothesis class H_k , $k=0,1,\dots,K-1$, and possessing joint p.d.f. $p_k\{f_1, f_2; ||\underline{u}||\}$. Then

$$Q_{m,n}(d;H_k) = \int_{E_m}^{E_{m+1}} \int_{E_n}^{E_{n+1}} p_k\{f_1, f_2; d\Delta L\} df_1 df_2, \quad (41)$$

[†] Strictly speaking this is not a p.d.f. but does provide a convenient normalization of the class-conditional log-likelihood functionals.

where E_l , $l=0,1,\dots,Q-1$ represents the lower boundaries of the quantization bins associated with level l , and ΔL represents the spatial sampling interval.

The likelihood functional defined by (39) has a simple interpretation as an inner product operation. More specifically, let $L_k(d)$ represent the $Q \times Q$ array with (m,n) element $l_k(m,n;d)$. Then (39) becomes

$$L_k\{P_{i,j}(d)\} = \langle P_{i,j}(d), L_k(d) \rangle ; \quad k=0,1,\dots,K-1 \quad , \quad (42)$$

where we have made use of the inner product

$$\langle A, B \rangle = \text{tr } AB^T \quad , \quad (43)$$

defined on the space of $Q \times Q$ matrices. The precomputed elements of $L_k(d)$ can be stored in a table and accessed as required. Computation of the inner product in (42) is relatively simple. The major computational burden is associated with computation of the $P_{i,j}(d)$ matrix. In the next section we describe a simple digital implementation of the log-likelihood discriminator which does not require explicit computation of $P_{i,j}(d)$. This approach is based upon 2-D Weiner filtering concepts. The result is a computationally efficient implementation as a 2-D recursive or infinite impulse response (IID) digital filter. Furthermore, the recursive implementation leads to a simple method of avoiding the block structure associated with the windowing operation.

VI. Digital Filter Implementation of Log-Likelihood Discriminator:

The log-likelihood functional described by (39) and the sequel requires a summation over gray levels or intensities. This can be replaced by a spatial summation and leads to a simple implementation as a 2-D digital filtering operation. In particular, recall that $p_{i,j}(m,n;d)$ is simply the number of times that gray levels m and n occur at a pair of points separated by d pixels within the window $W_{i,j}$, centered at pixel position (i,j) . It follows

that the class-conditional log-likelihood functional can be rewritten as

$$L_k\{F_{i,j};u\} = \sum_{(r,s) \in W_{i,j}} \left\{ \sum_{(u,v) \in S(r,s;d) \cap W_{i,j}}' \ell_k(f_{r,s}, f_{r+u, s+v}; d) \right\} \quad (44)$$

, k=0,1,...,K-1,

where $S(r,s;d)$ is the set of all points which are distance d from pixel position (r,s) . The outer summation in (44) is over the pixel positions (r,s) within the window $W_{i,j}$ centered at (i,j) while the inner summation is over the set $S(r,s;d) \cap W_{i,j}$ including only those points (u,v) within the window which simultaneously stand in the specified spatial relationship to pixel position (r,s) . Note that this latter summation can be obtained by searching over a circular neighborhood of radius of at most d units. We assume that appropriate bookkeeping has been employed to avoid double counting of pairs of points in the specified spatial relationship. This is indicated by the prime added to the inner spatial summation in (44).

At this point, it is convenient to define the quantity

$$g_k(r,s;d) \triangleq \sum_{(u,v) \in S(r,s;d) \cap W_{i,j}}' \ell_k(f_{r,s}, f_{r+u, s+v}; d) \quad ; k=0,1,...,K-1. \quad (45)$$

We are justified in expressing $g_k(r,s;d)$ as a function only of spatial coordinates (r,s) since once the sampled field $\{f_{i,j}\}_{i,j=1}^N$ has been observed this quantity is readily evaluated through (40) and the sequel. This assumes, of course, that boundary effects along the periphery of the window $W_{i,j}$ can be neglected; otherwise $g_k(r,s;d)$ would likewise depend upon the spatial index (i,j) . These boundary effects will be assumed negligible in what follows. This is a reasonable assumption if $d \ll M$ (recall the window $W_{i,j}$ is of size $(2M+1) \times (2M+1)$) which will generally be the case. It follows that (44) becomes

$$L_k\{i,j;d\} = \sum_{(r,s) \in W_{i,j}} g_k(r,s;d) ; \quad k=0,1,\dots,K-1 , \quad (46)$$

where we have found it convenient to suppress the functional dependence upon the observations $F_{i,j}$ and simply write $L_k\{i,j;d\}$ for $L_k\{F_{i,j};d\}$.

Consider now how the window size might be expected to influence performance of the log-likelihood discriminator. Clearly a large window size is desirable if the window covers an area of homogeneous texture, as this reduces the probability of classification error. As the window size is increased, however, it becomes more likely that the window will contain two or more regions of different texture classes thereby increasing the classification error. To arrive at a reasonable compromise between these conflicting factors the window has been allowed to be of infinite extent[†] but the sum in (46) is replaced by a weighted summation. The weights can then be chosen to provide diminishingly less weight to points the further they are from pixel position (i,j) . More specifically, we generalize (46) to the form

$$L_k\{i,j;d\} = \sum_r \sum_s h(i-r,j-s) g_k(r,s;d) ; \quad k=0,1,\dots,K-1 , \quad (47)$$

with $\{h(r,s)\}$ the weighting function. Note that (47) reduces to (46) under the assumption

$$h(r,s) = \begin{cases} 1 & ; \quad |r|, |s| \leq M \\ 0 & ; \quad \text{elsewhere} , \end{cases} \quad (48)$$

Furthermore, observe from (47) that $L_k\{i,j;d\}$ is simply the output of a 2-D digital filter with the sequence $\{g_k(r,s;d)\}$ as input. The weighting sequence $\{h(r,s)\}$ is the 2-D impulse response or point spread function of this filter.

[†] Note that this justifies our assumptions that boundary conditions are negligible in computing $g_k(r,s;d)$ from (45).

There are many heuristic arguments that can be developed for choosing an impulse response sequence $\{h(r,s)\}$. We have found it useful to formulate this choice as a 2-D Wiener filtering problem. More specifically, consider the filter input sequence defined by (45) as a function of a continuous spatial variable \underline{x} . The quantity $\{g_k(\underline{x};d), \underline{x} \in R^2\}$ is then a 2-D random field for each $k=0,1,\dots,K-1$, and parameterized by the distance d . Although the exact nature of this field is rather difficult to describe precisely, we will make some rather crude modeling assumptions which have led to some useful results. In particular, we assume that $g_k(\underline{x};d)$ can be represented as the sum of three separate components according to

$$g_k(\underline{x};d) = t(\underline{x}) + i(\underline{x}) + n(\underline{x}) \quad ; \quad \underline{x} \in R^2 \quad (49)$$

Here $t(\underline{x})$ represents a mean-value or signal component indicative of the true texture class. This component is constant over homogeneous texture regions and exhibits jumps or discontinuities at the boundaries between different textured regions. The component $i(\underline{x})$ represents an interference component the nature of which is similar to the texture within a region. This component reflects the pixel-to-pixel variations in $g_k(\underline{x};d)$ due to residual texture components. Finally, $n(\underline{x})$ represents an unavoidable noise component representing background noise, spurious image detail, quantization noise, etc.

In what follows the signal component $t(\underline{x})$ will be modeled in terms of a polygonal partition process as described in Section III. The edge density[†] λ_{te} , or equivalently λ_t , will be chosen on the basis of an assumed density for texture boundaries while the correlation $\rho_t=0$ will be chosen to reflect complete independence of texture in contiguous regions. Note that this latter assumption implies that the distance d has been chosen appropriately to maximize the discrimination ability; otherwise the signal process $t(\underline{x})$

† Again, by our subscripting convention λ_{te} represents the edge density of the field $t(\underline{x})$ along a randomly chosen line segment.

would be highly correlated in contiguous textured regions. The interference process $i(\underline{x})$, on the other hand, will be modeled as a texture process, either rectangular or polygonal, possessing much higher edge density and with parameters chosen to match the coarsest texture expected in the input image. In a sense this represents a worst case choice as the coarsest (i.e., lowest edge density) texture presents the most difficulty in separation from $t(\underline{x})$ by linear filtering. Finally, the noise field $n(\underline{x})$ is assumed a white noise field with power spectral density $S_{nn}(\Omega) = \sigma_n^2$.

It should be noted that the model specified by (49) is independent of both k and d , whereas in reality we would not expect this to be the case. Nevertheless this model has led to some useful and interesting results in selected computer experiments, some of which are described in the next section. The main justification for these modeling assumptions is based upon rather extensive empirical observations on typical realizations of $\{g_k(\underline{x};d), \underline{x} \in R^2\}$. Although the modeling is somewhat crude, it does provide some consideration of the relationship between the size of regions of constant texture and the coarseness of this texture in the design of the filtering operation. Specifically, there is an inherent tradeoff between the degree of smoothing of point-to-point variations of $g_k(\underline{x};d)$ and the ability of the generalized log-likelihood discriminator to distinguish small regions of homogeneous texture from contiguous regions. The Wiener filtering problem then is to determine the linear least mean-square estimate of $t(\underline{x})$ from the noisy observations represented by $g_k(\underline{x};d)$. The resulting 2-D Wiener filter possesses system transfer function.

$$H_0(\Omega) = \frac{S_{tt}(\Omega)}{S_{tt}(\Omega) + S_{ii}(\Omega) + S_{nn}(\Omega)} \quad , \quad (50)$$

where $S_{tt}(\Omega)$ and $S_{ii}(\Omega)$ are the power spectral densities of the true texture component $t(\underline{x})$ and the point-to-point interference component $i(\underline{x})$ respectively. As previously demonstrated, under our modeling assumptions, these quantities depend only upon the radial frequency Ω and hence the Wiener filter possesses this symmetry property. The system transfer function in (56) can be rewritten as

$$H_0(\Omega) = \frac{1}{1 + \frac{S_{ii}(\Omega)}{S_{tt}(\Omega)} + \frac{S_{nn}(\Omega)}{S_{tt}(\Omega)}} \quad (52)$$

which suggests defining the parameters γ_i and γ_n as the ratio of interference and noise powers to the power in the texture process respectively. These parameters provide a measure of the degree of degradation by interference from residual texture components and salt-and-pepper noise. More specifically, we have

$$\gamma_i \triangleq \sigma_i^2 / \sigma_t^2 \quad (53a)$$

while

$$\gamma_n \triangleq \sigma_n^2 / \sigma_t^2 \quad (53b)$$

so that the Wiener filter transfer function $H_0(\Omega)$ is completely determined in terms of the quantities $\gamma_i, \gamma_n, \lambda_i, \rho_i, \lambda_t$ and ρ_t . In any particular application these can be estimated empirically or on the basis of a priori knowledge concerning the texture classes to be discriminated.

The preceeding description of the optimum linear filtering operation is for a continuous spatial domain; we have access only to sampled data so that a digital implementation is required. In particular, we seek a 2-D digital filter with system transfer function $H_0(z_1, z_2)$ whose frequency response^{††} approximates $H_0(\Omega)$. While there are many digital implementations available,

[†] Actually $\rho_t = 0$ in the work described here.

^{††} The frequency response of the 2-D digital filter is simply $H_0(z_1, z_2)$ evaluated for $z_i = e^{j\omega_i}$, $i=1,2$. We assume the spatial frequency variable ω_i is measured in units of radius per sample distance.

our approach has been to make use of a 2-D infinite impulse response (IIR) digital filter whose point spread function exhibits four-quadrant symmetry. The choice of an IIR filter was dictated by the computational economies which result from the inherent recursive nature of the computations involved. Similarly, the restriction to four-quadrant symmetry for $\{h(r,s)\}$ follows from the requirement that the log-likelihood discriminator not exhibit any directional sensitivities.

The IIR filters will be assumed to possess rational system transfer functions of the form

$$H_0(z_1, z_2) = \frac{\sum_{i=0}^{M_b} \sum_{j=0}^{N_b} b_{ij} z_1^{-i} z_2^{-j}}{1 + \sum_{\substack{i=0 \\ i \neq j \neq 0}}^{M_a} \sum_{j=0}^{N_a} a_{ij} z_1^{-i} z_2^{-j}} \quad (54)$$

In particular, the output sequence $\{y_{i,j}\}$ in response to $\{x_{i,j}\}$ as input can be obtained recursively according to

$$y_{m,n} = - \sum_{\substack{i=0 \\ i \neq j \neq 0}}^{M_a} \sum_{j=0}^{N_a} a_{ij} y_{m-i, n-j} + \sum_{i=0}^{M_b} \sum_{j=0}^{N_b} b_{ij} x_{m-i, n-j}; \quad m, n \geq 0 \quad (55)$$

We will assume that the geometry is such that this corresponds to a stable filter recursing from the upper left-hand corner. Observe that the resulting filter will have nonzero impulse response only in the lower right quadrant.

As mentioned previously, it is highly desirable that the digital filter implementation of the log-likelihood discriminator exhibit four-quadrant symmetry in its impulse response or point spread function. One method for achieving a point spread function with this inherent symmetry is to allow repeated application of the same filter recursing from each of the four corners. If $\{h_0(i,j)\}$ represents the point spread function associated with a single application of the filter specified by (54) then the composite filter possesses

point spread function as indicated in Fig. 16. The corresponding system transfer function of the composite filter is then

$$H(z_1, z_2) = z_1^{-1/2} z_2^{-1/2} H_1(z_1, z_2), \quad (56)$$

where

$$H_1(z_1, z_2) \triangleq H_0(z_1, z_2) + z_1 H_0(z_1^{-1}, z_2) + z_2 H_0(z_1, z_2^{-1}) + z_1 z_2 H_0(z_1^{-1}, z_2^{-1}). \quad (57)$$

It follows that the frequency response of $H(z_1, z_2)$ is identical to that of $H_1(z_1, z_2)$ up to an unimportant linear phase term. In choosing $H_1(z_1, z_2)$ to provide an approximation to $H_0(\Omega)$ for $z_i = e^{j\omega_i}$, $i=1,2$, we have restricted attention to the case where $H_0(z_1, z_2)$ is a simple first-order section of the form

$$H_0(z_1, z_2) = A \left(\frac{1 + b_{10}(z_1^{-1} + z_2^{-1}) + b_{11}z_1^{-1}z_2^{-1}}{1 + a_{10}(z_1^{-1} + z_2^{-1}) + a_{11}z_1^{-1}z_2^{-1}} \right). \quad (58)$$

This choice insures zero frequency response at the origin and symmetry of the corresponding point spread function about a line at 45° to the axes, i.e., $h_0(i,j) = h_0(j,i)$. Similar properties extend, of course, to the composite filter represented by $H(z_1, z_2)$. A computer program has been written for determining the four coefficients $a_{10}, a_{11}, b_{10}, b_{11}$ and the gain A according to an iterative gradient procedure to result in a frequency response for $H_1(z_1, z_2)$ which provides a least mean-square approximation to the desired response $H_0(\Omega)$. The details of this program are described in [29].

In Table I we summarize the results of this iterative digital filter design approach for selected values of $\gamma_i, \rho_i, \lambda_i, \rho_t$, and λ_t all with $\gamma_n = -10\text{dB}$. Here we have found it convenient to classify the interference characteristics as weak, moderate or strong depending upon the value of γ_i . The parameters chosen here are particularly relevant to some experimental results to be described in the next section.

Interference Characteristic	λ_i	ρ_i	λ_t	ρ_t	A	a_{10}	a_{11}	b_{10}	b_{11}
Weak	0.16	0.0	0.0125	0.0	0.8131	-0.9743	0.9524	0.2915	-0.9098
Moderate	0.16	0.0	0.0125	0.0	0.2032	-0.9493	0.9036	-0.0375	-0.1761
Strong	0.16	0.5	0.0125	0.0	0.4220	-0.9605	0.9220	-0.8796	0.8432

Table 1

Typical Filter Parameters for $\gamma_n = -10\text{dB}$

For the three cases described in Table 1, the corresponding power spectral densities $S_{tt}(\Omega)$ and $S_{ii}(\Omega) + S_{nn}(\Omega)$, together with the resulting Wiener filter response $H_0(\Omega)$, are plotted in Fig. 17 as a function of the radial frequency variable Ω . Observe the lowpass behavior in all cases with the selectivity increasing with increasing levels of interference. Finally, in Fig. 18 we illustrate 3-D plots of the desired Wiener filters and the resulting digital approximations. In all cases, the closest corner represents the point[†] $[-\pi, \pi]$ while the farthest corner represents the point $[\pi, \pi]$. The left-hand column shows the desired responses while the right-hand column illustrates the responses exhibited by the digital approximations. Note that in all cases the lowpass nature of the optimum filter has been preserved and a fair degree of symmetry has been retained.

[†] Frequency axes for ω_i , $i=1,2$, have been normalized to the range $[-\pi, \pi]$ with the endpoints corresponding to \pm the folding frequency, i.e., half the sampling rate.

VII. Experimental Results:

Typical performance results for selected texture discriminators are provided in Fig. 19. Here Fig. 19a illustrates the original image which consists of realizations of three distinct rectangular partition processes for various parameter choices. The NW and NE corners have $\lambda=0.16$, $\rho=0.0$, and $\lambda=0.32$, $\rho=0.5$ respectively. These values were carefully chosen, according to previous comments, to result in identical second-moment properties. As a result these two fields cannot be discriminated on the basis of autocorrelation functions and/or power spectral densities alone. The field in the S corner has $\lambda=0.32$ while $\rho=0.0$. Since it possesses the same edge density as the field in the NE corner, these two textures cannot be discriminated on the basis of edge density alone. Although somewhat contrived, we feel that this problem provides a real challenge to texture discrimination algorithms.

Three log-likelihood discriminators were designed using the filter parameters corresponding to the three entries in Table 1. The choice $\lambda_i=0.16$ corresponds to the coarsest texture in Fig. 19a while λ_t was chosen to approximate the density of texture boundaries. Recall that the edge density in this case is given by $\lambda_{te}=\lambda_t/\pi$ edges per pixel so that for this choice there would be on average approximately one texture transition along the boundary of 256x256 image. This approximates the situation illustrated in Fig. 19a.

In Fig. 19b we illustrate the performance[†] of the log-likelihood texture discriminator for the case of moderate interference, i.e., the middle entry in Table 1. The value of d used here was $d=3$. Ideally, this quantity should be chosen such that $d=1/\lambda_e$ (recall $\lambda_e=4\lambda/\pi$ for the rectangular partition process) to provide maximum discrimination ability. In situations, such as that presented in Fig. 19a, where there are more than one value of edge density

[†] In all experimental results reported in this section the images were uniformly quantized to $Q=64$ levels.

associated with the texture samples to be discriminated, a reasonable choice is to choose $d \approx 1/\bar{\lambda}_e$ where $\bar{\lambda}_e$ represents the average edge density over all texture classes. For the present case we have $\bar{\lambda}_e = .306$ and hence the choice $d=3$ provides the desired approximation. Studies have indicated that performance is not a sensitive function of d in the range $2 \leq d \leq 5$, although the choice $d=3$ appeared to be about optimum. As indicated by Fig. 19b, the log-likelihood discriminator does an excellent job of discriminating the three texture regions except in the vicinity of either texture or image boundaries. This performance, however, can be improved as we demonstrate subsequently.

Included in Fig. 19 for comparison purposes we have indicated the performance of alternative more conventional texture discrimination schemes. In Fig. 19c we demonstrate the performance of a conventional correlation discriminator. This algorithm implements a threshold test on a least-squares estimate of the correlation of pixels separated by distance d . The optimum threshold has been chosen empirically on the basis of histogram techniques. While this approach is useful in discriminating the texture in the S corner from that in either the NW or NE corner, it cannot discriminate between the NW and NE regions due to the fact they possess identical second-moment properties. As a partial remedy to this situation we have devised a discriminant that employs both correlation and edge density information. Since this discriminator appears sufficiently interesting itself, we have provided details on its implementation in the Appendix. Using this correlation/edge density discriminator some degree of success has been achieved in discriminating between the NW and NE regions as illustrated by the results in Fig. 19d. The results are, however, generally inferior to the performance of the log-likelihood discriminator.

In order to assess the sensitivity of the performance of the log-likelihood discriminator to our modeling assumptions, we have applied the three designs

described in Table 1 to the original image in Fig. 19c. In all cases we have taken $d=3$. The results are illustrated in Fig. 20 and provide some indication of how performance depends upon the choice of filtering function. In Fig. 20b we illustrate the result under the assumption of weak interference ($\gamma_i=6\text{dB}$, $\rho_i=0.0$). The boundaries between the three different texture regions, which are actually straight lines, are irregular and small patches in each region have been misclassified. In Fig. 20c we illustrate performance, as in Fig. 19b, for moderate interference ($\gamma_i=0\text{dB}$, $\rho_i=0.0$). The boundaries between regions are smoother and the misclassified regions are smaller. Finally, in Fig. 20d we illustrate performance for strong interference ($\gamma_i=6\text{dB}$, $\rho_i=0.5$). The boundaries are now much straighter and the misclassified patches have disappeared. However, the point of intersection of the three boundaries has become ill-defined as a result of the additional smoothing introduced to reduce the interference. These results are useful in illustrating the tradeoffs in choosing the strength of the interference.

VIII. Summary and Conclusions:

We have described a new approach to texture discrimination which appears to offer considerable improvement over existing approaches under specific, although realistic, stochastic modeling assumptions. While initial results have been rather encouraging, much more work remains in establishing the efficacy of this approach.

For example, we have described a Wiener filtering approach to the 2-D digital filter implementation of the class-conditional generalized log-likelihood functionals. Clearly, other approaches to the digital filter design problem are possible within the general structure of the texture discriminant proposed here. Several alternative approaches are presently under investigation.

A more fundamental difficulty with this approach, however, is the requirement for knowledge of the model parameters for each of the texture classes known to be acting in any discrimination application. This knowledge is required in constructing the inputs $g_k(i,j;d), k=0,1,\dots,K-1$, to the digital filters which generate the class-conditional log-likelihood functionals. We assumed this knowledge, for example, in the experiments described in the preceding section. In practice it may be possible to obtain crude estimates of these parameters either on the basis of a priori knowledge or derived from the data itself. These estimates may be sufficiently accurate to provide useful discrimination performance. An alternative may be to use a range of "prototype" stochastic texture models which span the range of textures of interest. Use of these "prototype" texture models in constructing corresponding class-conditional log-likelihood functionals may result in useful discrimination ability. Both of these approaches are being pursued.

Finally, the proposed texture discriminant is intimately related to our modeling assumptions. When applied to realizations of stochastic models for which it was developed, the performance is excellent. Assessment of the true value of this approach, however, will require relative performance evaluation vis-à-vis existing approaches on real-world data. This relative evaluation should be respect to both accuracy and computational cost.

APPENDIX

CORRELATION/EDGE DENSITY DISCRIMINATOR

The correlation/edge density discriminator bases its decisions on maximum likelihood estimates $\hat{\rho}, \hat{\lambda}$ of the correlation of points separated by a distance d and the density of edges respectively. A linear discriminator has been used to separate the $\hat{\rho}, \hat{\lambda}$ plane into appropriate regions. This discriminator parallels the log-likelihood discriminator to the extent that observations of pairs of points within a window are assumed independent and furthermore the windowing operation is replaced by a weighted window implemented as a 2-D recursive digital filter. Here, however, the likelihood functionals are maximized over a continuum of values rather than a finite set of hypothesis.

The maximum likelihood estimate of the correlation will be formed under the assumption that observations at pairs of points are zero mean jointly Gaussian random variables. The p.d.f. of N independent observations of two jointly Gaussian random variables conditioned upon their correlation and variance is given by

$$p\{(x_i, y_i), i=1, N | \rho, \sigma\} = \frac{1}{[2\pi\sigma^2(1-\rho^2)]^{1/2}}^N \exp \left\{ - \frac{\sum_{i=1}^N (x_i^2 - 2\rho x_i y_i + y_i^2)}{2\sigma^2(1-\rho^2)} \right\} \quad (A-1)$$

Here the N points under consideration would be the set of pairs of pixels within a window W and separated by a distance d while the random variables x and y correspond to a pair of values taken on by each pair of pixels.

The values of ρ and σ for which the above quantity is maximized are their maximum likelihood estimates. It will prove more convenient to maximize the logarithm of the above as given by

$$\begin{aligned} \ell(\rho, \sigma) = & -N \ln(2\pi\sigma^2) - \frac{N}{2} \ln(1-\rho^2) \\ & - \frac{\sum_{i=1}^N (x_i^2 - 2\rho x_i y_i + y_i^2)}{2\sigma^2(1-\rho^2)} \end{aligned} \quad (A-2)$$

Upon setting the partials of the above expression with respect to ρ and σ to zero and solving for ρ and σ we obtain the estimates

$$\hat{\sigma}^2 = \frac{1}{N} \sum_{i=1}^N (x_i^2 + y_i^2) / 2 \quad , \quad (A-3a)$$

and

$$\hat{\rho} = \frac{1}{N \hat{\sigma}^2} \sum_{i=1}^N x_i y_i \quad . \quad (A-3b)$$

As in the log-likelihood discriminator the summations above over a window were replaced by a low pass filter.

The maximum likelihood estimate of the edge density will be made under the assumption that the occurrence of edges along an arbitrarily placed line can be described as event times of a Poisson process. Then the probability of observing N_0 intervals of length d with no events and N_e intervals with one or more events under the assumption that the edge density is λ is given by [15]

$$P(N_0, N_e | \lambda) = \frac{(N_0 + N_e)!}{N_0! N_e!} [\exp(-\lambda d)]^{N_0} [1 - \exp(-\lambda d)]^{N_e} \quad . \quad (A-4)$$

It will prove convenient to work with the logarithm of the above as

$$\ell(N_0, N_e | \lambda) = \ln \frac{(N_0 + N_e)!}{N_0! N_e!} + N_0(-\lambda d) + N_e \ln[1 - \exp(-\lambda d)] \quad (A-5)$$

Setting the derivative of the above with respect to λ to zero and solving for λ yields

$$\hat{\lambda} = \frac{1}{d} \ln \beta_0, \quad (A-6)$$

where $\beta_0 = N_0 / (N_0 + N_e)$ is the fraction of intervals with no events. In fact, the quantity used in the discriminator was not $\hat{\lambda}$ but rather an estimate of β_0

formed by passing the output of a simple edge detector through the lowpass filter used for the log-likelihood discriminator. The edge detector simply applies a threshold to the difference between the gray levels at pairs of pixels separated by distance d . Here the value of d is the same as that used by the log-likelihood discriminator (3 pixels) while the lowpass filter is the Wiener filter designed under the assumption of moderate interference. Additional details can be found in [29].

References

1. R. M. Haralick, K. Shanmugam, and I. Dinstein, "Textural Features for Image Classification", *IEEE Trans. Syst. Man, and Cybern.*, vol. SMC-3, pp. 610-621, Nov. 1973.
2. R. M. Haralick, "Automatic Remote Sensing Image Processing", in Digital Picture Analysis, A. Rosenfeld, Ed., Springer-Verlag, Berlin, 1976, pp. 5-63.
3. R. M. Pickett, "Visual Analysis of Texture in the Detection and Recognition of Objects" in Picture Processing and Psychopictorics, B. S. Lipkin and A. Rosenfeld, Ed.'s, Academic Press, New York, 1970, pp. 289-308.
4. J. K. Hawkins, "Textural Properties for Pattern Recognition", in Picture Processing and Psychopictorics, B. S. Lipkin and A. Rosenfeld, Ed.'s, Academic Press, New York, 1970, pp. 347-370.
5. W. K. Pratt, Digital Image Processing, Wiley-Interscience, New York, 1978, pp. 503-511.
6. S. W. Zucker, "Toward a Model of Texture", *Comput. Graph. Image Processing*, vol. 5, pp. 190-202, 1976.
7. S. Y. Lu and K. S. Fu, "A Syntactic Approach to Texture Analysis", *Comput. Graph. Image Processing*, vol. 7, pp. 303-330, 1978.
8. R. M. Haralick, "Statistical and Structural Approaches to Texture", *Proc. of IEEE*, vol. 67, pp. 786-804, May 1979.
9. J. Weszka, C. Dyer, and A. Rosenfeld, "A Comparative Study of Texture Measures for Terrain Classification", *IEEE Trans. Syst., Man, and Cybern.*, vol. SMC-6, pp. 269-285, April 1976.
10. B. Julesz, "Visual Pattern Discrimination", *IRE Trans. Inform. Theory*, vol. IT-8, pp. 84-92, Feb. 1962.
11. B. Julesz, E. N. Gilbert, L. A. Shepp, and H. L. Frisch, "Inability of Humans to Discriminate Between Visual Textures that Agree in Second-Order Statistics-Revisited", *Perception*, vol. 2, pp. 391-405, 1973.
12. W. K. Pratt, O. D. Faugeras, and A. Gagalowicz, "Visual Discrimination of Stochastic Texture Fields", *IEEE Trans. Syst., Man, and Cybern.*, vol. SMC-8, pp. 796-804, Nov. 1978.
13. B. J. Schachter, A. Rosenfeld, and L. S. Davis, "Random Mosaic Models for Textures", *IEEE Trans. Syst., Man, and Cybern.*, vol. SMC-8, pp. 694-702, Sept. 1978.

14. E. Wong, "Two-Dimensional Random Fields and the Representation of Images", SIAM J. Appl. Math., vol. 16, pp. 756-770, 1968.
15. A. Papoulis, Probability, Random Variables and Stochastic Processes, McGraw-Hill, New York, 1965, chap. 11.
16. S. Bochner, Lectures on Fourier Integrals, Annals of Math. Studies, No. 42, Princeton Univ. Press, Princeton, NJ, 1959, pp. 235-238.
17. A. Papoulis, "Optical Systems, Singularity Functions, Complex Hankel Transforms", J. Opt. Soc. Amer., vol. 57, pp. 207-213, 1967.
18. A. Papoulis, Systems and Transforms with Applications in Optics, McGraw-Hill, New York, 1968.
19. B. H. McCormick and S. N. Jayaramamurthy, "Time Series Model for Texture Synthesis", Int. J. Comput. Inform. Sci., vol. 3, pp. 329-343, Dec. 1974.
20. B. H. McCormick and S. N. Jayaramamurthy, "A Decision Theory Method for the Analysis of Texture", Int. J. Comput. Inform. Sci., vol. 4, pp. 1-38, March 1978.
21. J. T. Tou and Y. S. Chang, "An Approach to Texture Pattern Analysis and Recognition", in Proc. 1976 IEEE Conf. on Decision and Control, pp. 398-403, Dec. 1976.
22. P. Brodatz, Texture: A Photograph Album for Artists and Designers, Dover, New York, 1956.
23. D. L. Snyder, Random Point Processes, Wiley, New York, 1975.
24. E. Parzen, Stochastic Processes, Holden-Day, San Francisco, CA., 1962.
25. E. Cinlar, Introduction to Stochastic Processes, Prentice-Hall, Englewood Cliffs, NJ., 1975.
26. W. Feller, An Introduction to Probability and Its Applications, vol. 2, Wiley, New York, 1971.
27. J. W. Modestino and R. W. Fries, "A Generalization of the Random Telegraph Wave", submitted to IEEE Trans. on Inform. Theory.
28. J. W. Modestino and R. W. Fries, "Stochastic Models for Images with Applications", in Proc. of NATO Advanced Institute on Pattern Recognition and Signal Processing, C. H. Chen, Ed., Sijthoff and Noordhoff, Alphen aan den Rijn, The Netherlands, 1978, pp. 225-249.
29. R. W. Fries, "Theory and Applications of a Class of Two-Dimensional Random Fields", Ph. D. thesis, Electrical and Systems Engineering Dept., RPI, Troy, N.Y., in preparation.

30. J. W. Modestino and R. W. Fries, "Construction and Properties of a Useful Two-Dimensional Random Field", to appear in IEEE Trans. on Inform. Theory.
31. J. W. Modestino and R. W. Fries, "Edge Detection in Noisy Images Using Recursive Digital Filtering", Comput. Graph. Image Processing, vol. 6, pp. 409-433, 1977.
32. J. W. Modestino, R. W. Fries, and D. G. Daut, "A Generalization of the Two-Dimensional Random Checkerboard Process", J. Opt. Soc. Am., vol. 69, pp. 897-906, June 1979.
33. H. L. Van Trees, Detection, Estimation, and Modulation Theory; Part I, Wiley, New York, 1968.
34. K. Fukunaga, Introduction to Statistical Pattern Recognition, Academic Press, New York, 1972.

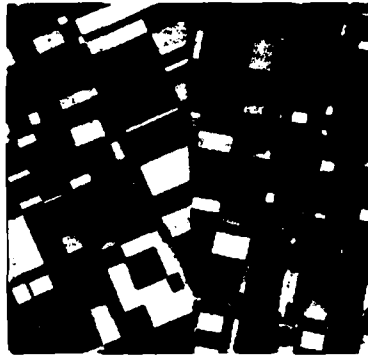


Figure 1

Realizations of Two Random Fields Possessing
Identical Power Spectral Densities;
L, $\lambda=0.08$, $\rho=0.0$; R, $\lambda=0.16$, $\rho=0.5$

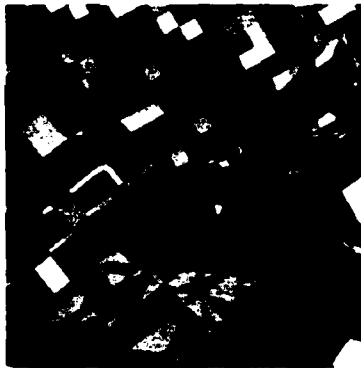


Figure 2

Selected Realizations of Random Fields
Possessing Identical Edge Density;
W, Rectangular $v=1$, $\lambda=0.08$, $\rho=0.0$,
N, Rectangular $v=\infty$, $\lambda=0.08$, $\rho=0.0$,
SE, Polygonal $v=1$, $\lambda=0.32$, $\rho=0.0$.

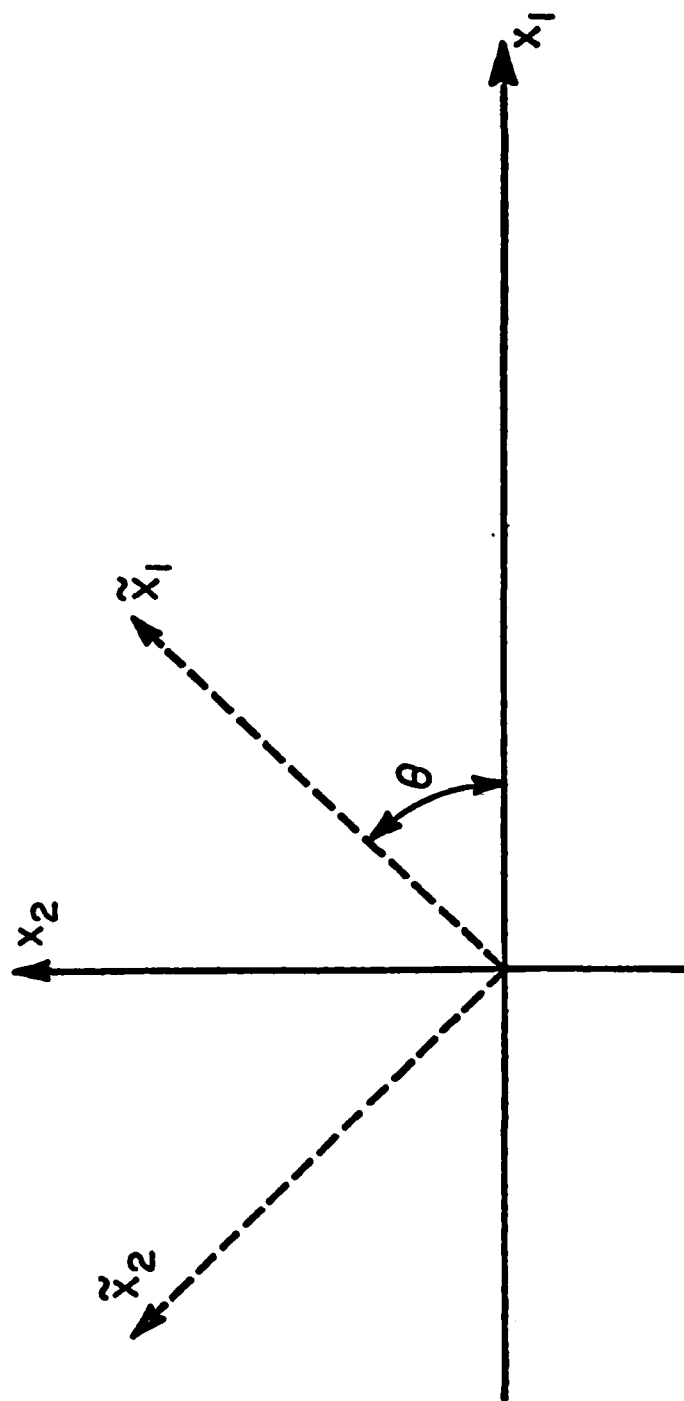
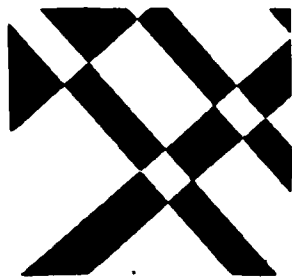
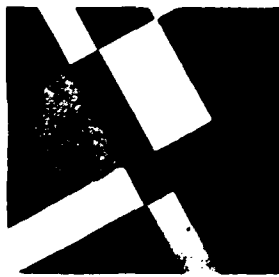


Figure 3
Rotation of Cartesian Coordinate Axes



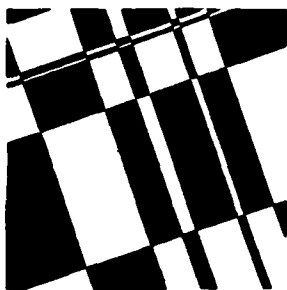
a.) $\lambda=0.0125, \rho=-0.9$



b.) $\lambda=0.0125, \rho=0.0$



c.) $\lambda=0.0125, \rho=0.5$



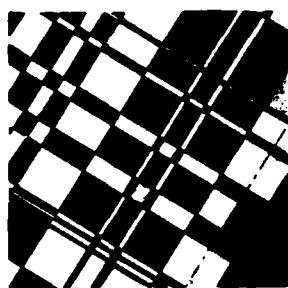
d.) $\lambda=0.025, \rho=-0.9$



e.) $\lambda=0.025, \rho=0.0$



f.) $\lambda=0.025, \rho=0.5$



g.) $\lambda=0.05, \rho=-0.9$



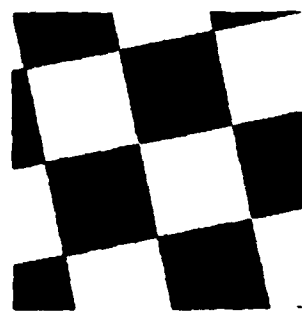
h.) $\lambda=0.05, \rho=0.0$



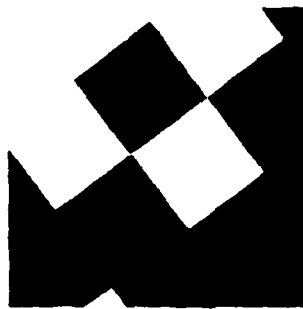
i.) $\lambda=0.05, \rho=0.5$

Figure 4

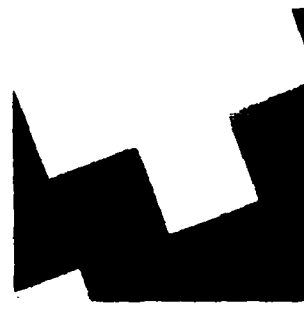
Selected Realizations of Random Field
Generated by Poisson Partitions



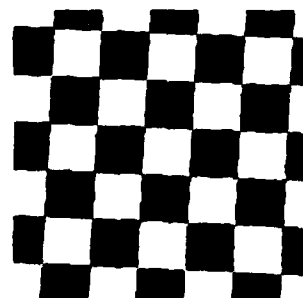
a.) $\lambda=0.0125$, $\rho=-0.9$



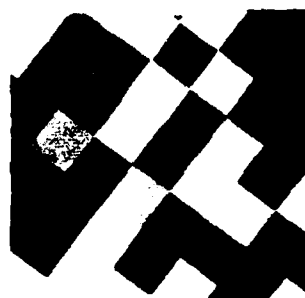
b.) $\lambda=0.0125$, $\rho=0.0$



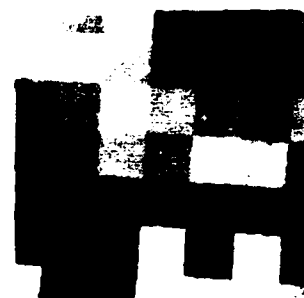
c.) $\lambda=0.0125$, $\rho=0.5$



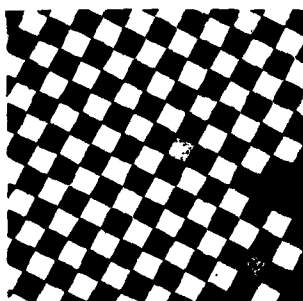
d.) $\lambda=0.025$, $\rho=-0.9$



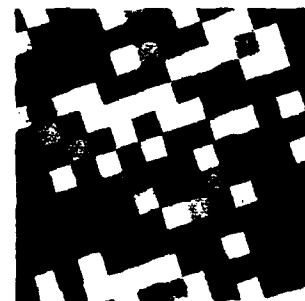
e.) $\lambda=0.025$, $\rho=0.0$



f.) $\lambda=0.025$, $\rho=0.5$



g.) $\lambda=0.05$, $\rho=-0.9$



h.) $\lambda=0.05$, $\rho=0.0$



i.) $\lambda=0.05$, $\rho=0.5$

Figure 5

Selected Realizations of Random Field
Generated by Periodic Partitions



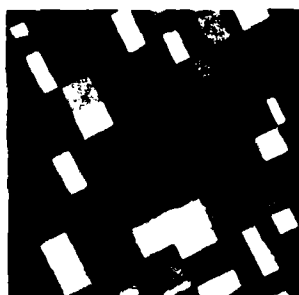
a) $\nu=1$



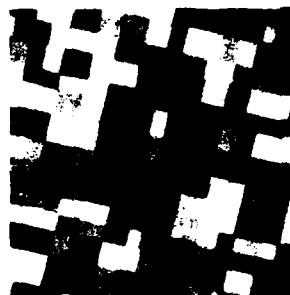
b) $\nu=2$



c) $\nu=4$



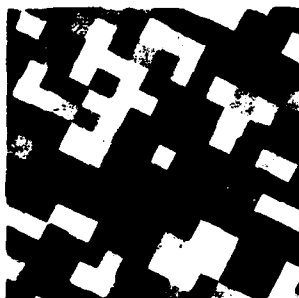
d) $\nu=8$



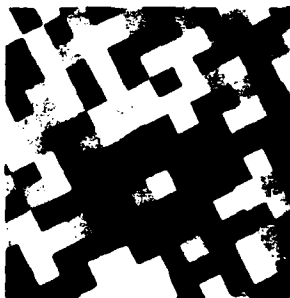
e) $\nu=16$



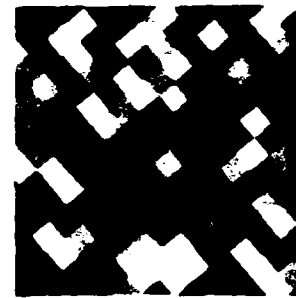
f) $\nu=32$



g) $\nu=64$



h) $\nu=128$



i) $\nu=\infty$

Figure 6

Selected Realizations of Random Field Generated
by Stationary Renewal Point Process Possessing
Gamma Distributed Interarrival Distribution and
with $\lambda=0.05$ and $\rho=0.0$

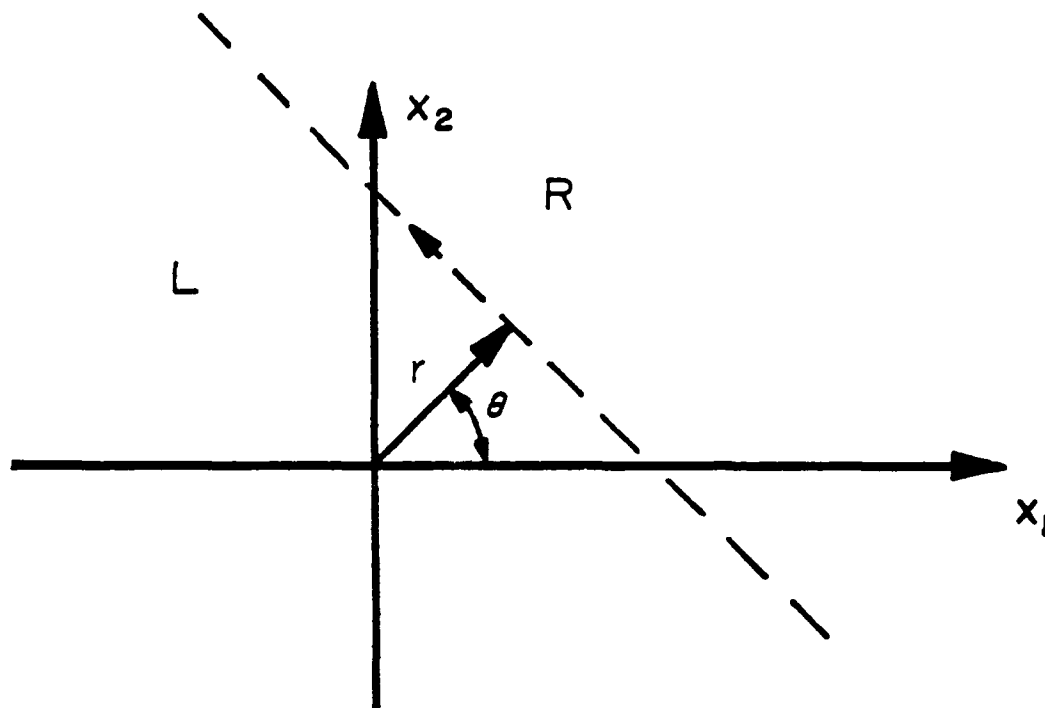
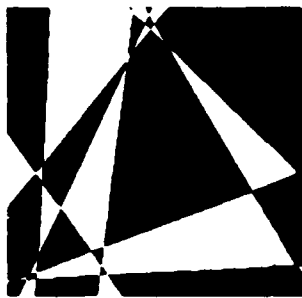
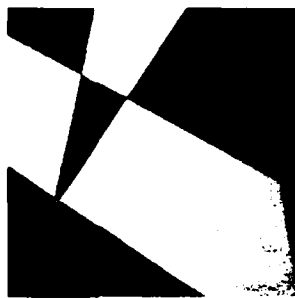


Figure 7
Parameterization of Directed Line Segment



a) $\lambda_e = 0.0125, \rho = -0.9$



b) $\lambda_e = 0.0125, \rho = 0.0$



c) $\lambda_e = 0.0125, \rho = 0.5$



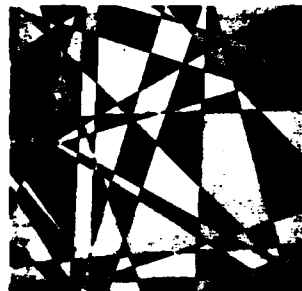
d) $\lambda_e = 0.025, \rho = -0.9$



e) $\lambda_e = 0.025, \rho = 0.0$



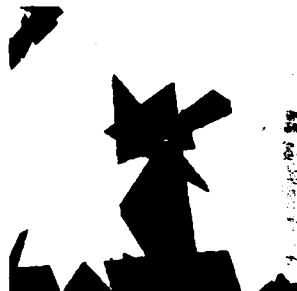
f) $\lambda_e = 0.025, \rho = 0.5$



g) $\lambda_e = 0.05, \rho = -0.9$



h) $\lambda_e = 0.05, \rho = 0.0$



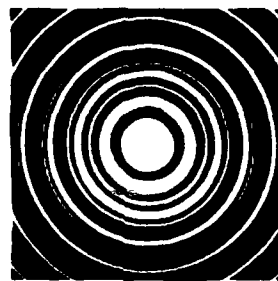
i) $\lambda_e = 0.05, \rho = 0.5$

Figure 8

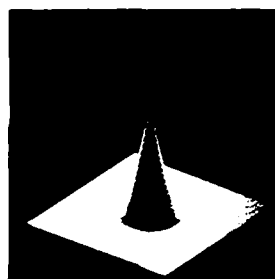
Selected Realizations of Random Field
Generated by Polygonal Partitions



a) Autocorrelation Function
 $\rho = -0.5$



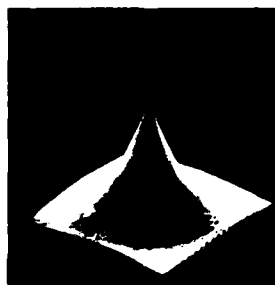
b) Power Spectral Density
 $\rho = -0.5$



c) Autocorrelation Function
 $\rho = 0$



d) Power Spectral Density
 $\rho = 0$



e) Autocorrelation Function
 $\rho = 0.5$



f) Power Spectral Density
 $\rho = 0.5$

Figure 9
Autocorrelation Function and Power Spectral Density
of 2-D Random Checkerboard Process Generated by
Periodic Partitions

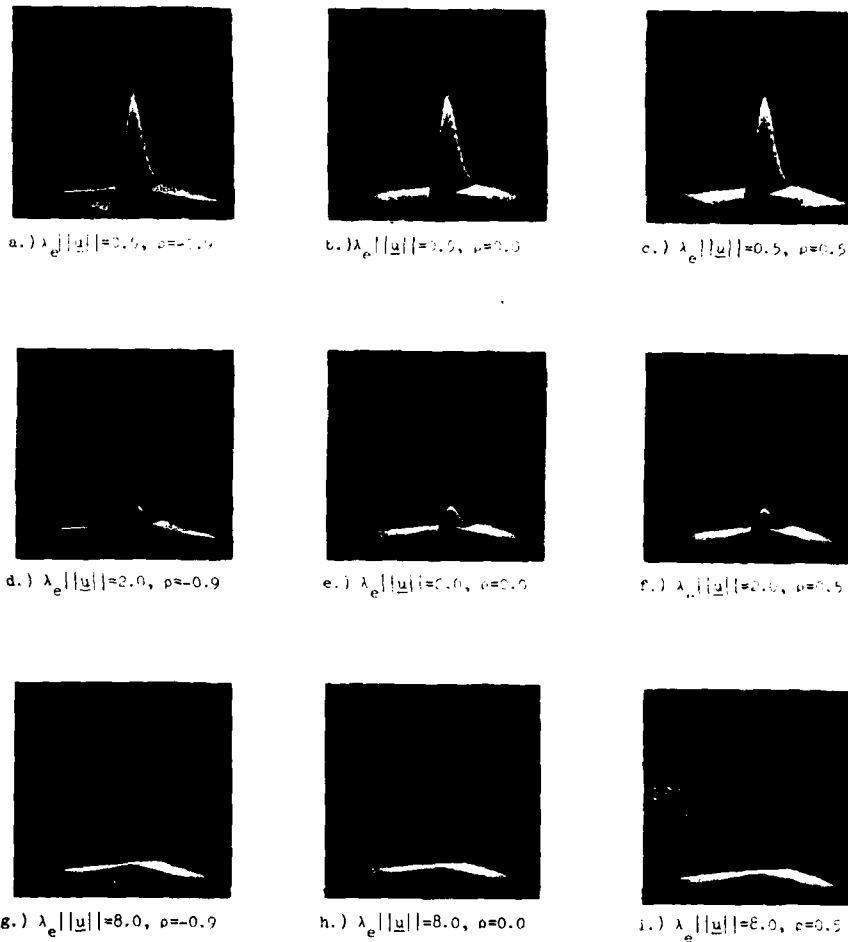


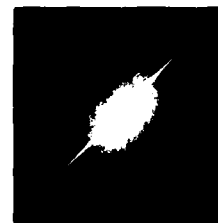
Figure 10
 Selected Joint Probability Density Functions
 for Rectangular Partition Process, $v=1$



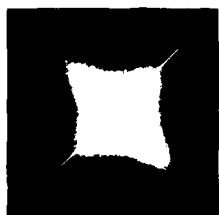
a.) $\lambda_e ||\underline{u}|| = 0.5, \rho = -0.9$



b.) $\lambda_e ||\underline{u}|| = 0.5, \rho = 0.0$



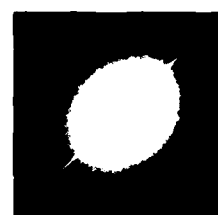
c.) $\lambda_e ||\underline{u}|| = 0.5, \rho = 0.5$



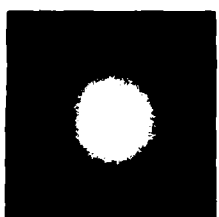
d.) $\lambda_e ||\underline{u}|| = 2.0, \rho = -0.9$



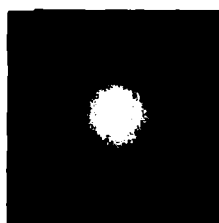
e.) $\lambda_e ||\underline{u}|| = 2.0, \rho = 0.0$



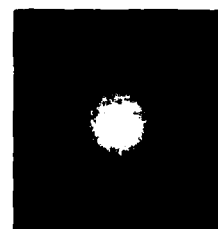
f.) $\lambda_e ||\underline{u}|| = 2.0, \rho = 0.5$



g.) $\lambda_e ||\underline{u}|| = 8.0, \rho = -0.9$



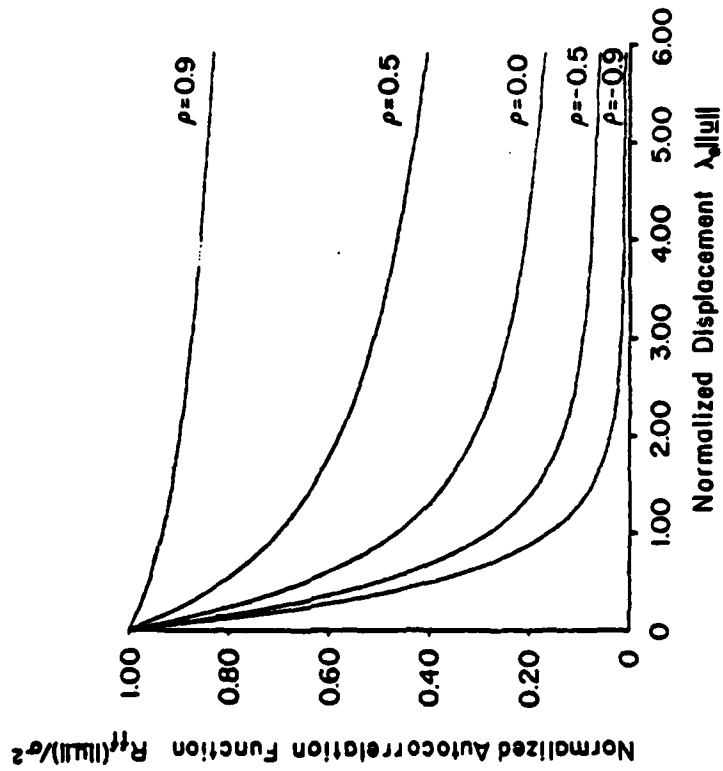
h.) $\lambda_e ||\underline{u}|| = 8.0, \rho = 0.0$



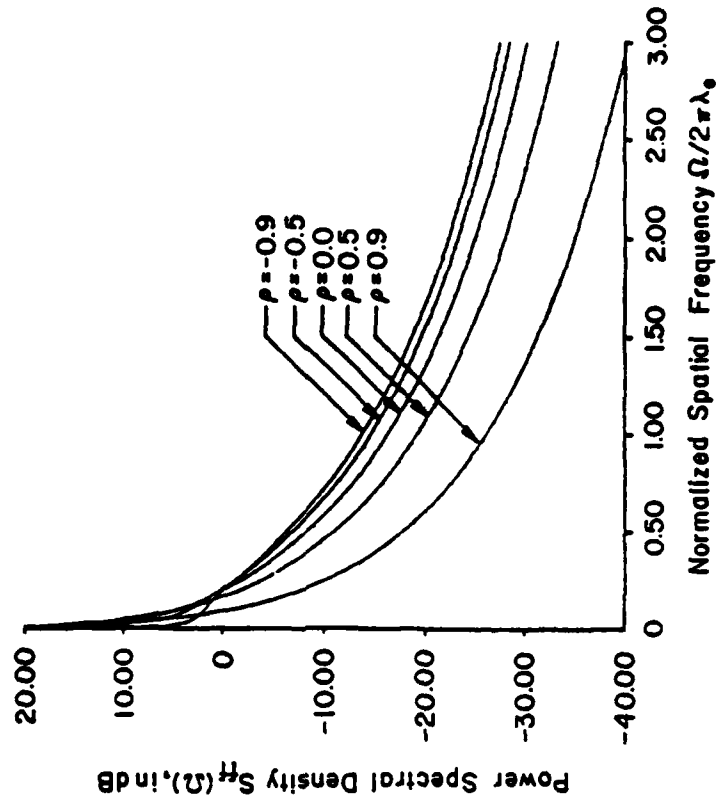
i.) $\lambda_e ||\underline{u}|| = 8.0, \rho = 0.5$

Figure 11

Intensity Plots of Logarithm of Selected
Joint Probability Density Functions
for Rectangular Partition Process, $v=1$



a.) NORMALIZED AUTOCORRELATION FUNCTION



b.) POWER SPECTRAL DENSITY

Figure 12
Autocorrelation Function and Power Spectral Density
of 2-D Random Field Generated by Polygonal Partitions



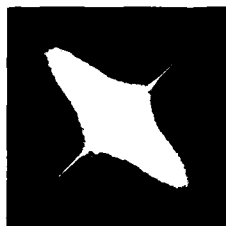
a.) $\lambda_e ||\underline{u}||=0.5, \rho=-0.9$



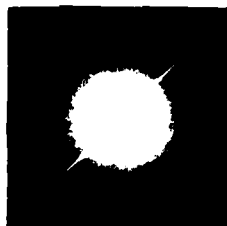
b.) $\lambda_e ||\underline{u}||=0.5, \rho=0.0$



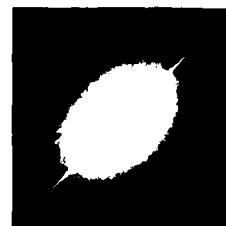
c.) $\lambda_e ||\underline{u}||=0.5, \rho=0.5$



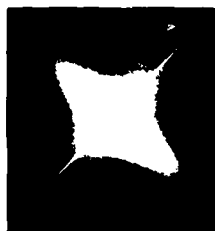
d.) $\lambda_e ||\underline{u}||=2.0, \rho=-0.9$



e.) $\lambda_e ||\underline{u}||=2.0, \rho=0.0$



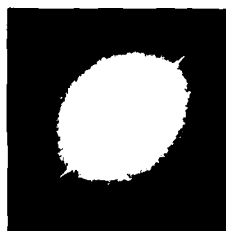
f.) $\lambda_e ||\underline{u}||=2.0, \rho=0.5$



g.) $\lambda_e ||\underline{u}||=8.0, \rho=-0.9$



h.) $\lambda_e ||\underline{u}||=8.0, \rho=0.0$



i.) $\lambda_e ||\underline{u}||=8.0, \rho=0.5$

Figure 13

Intensity Plots of Logarithm of Selected Joint
Probability Density Functions for Polygonal
Partition Process

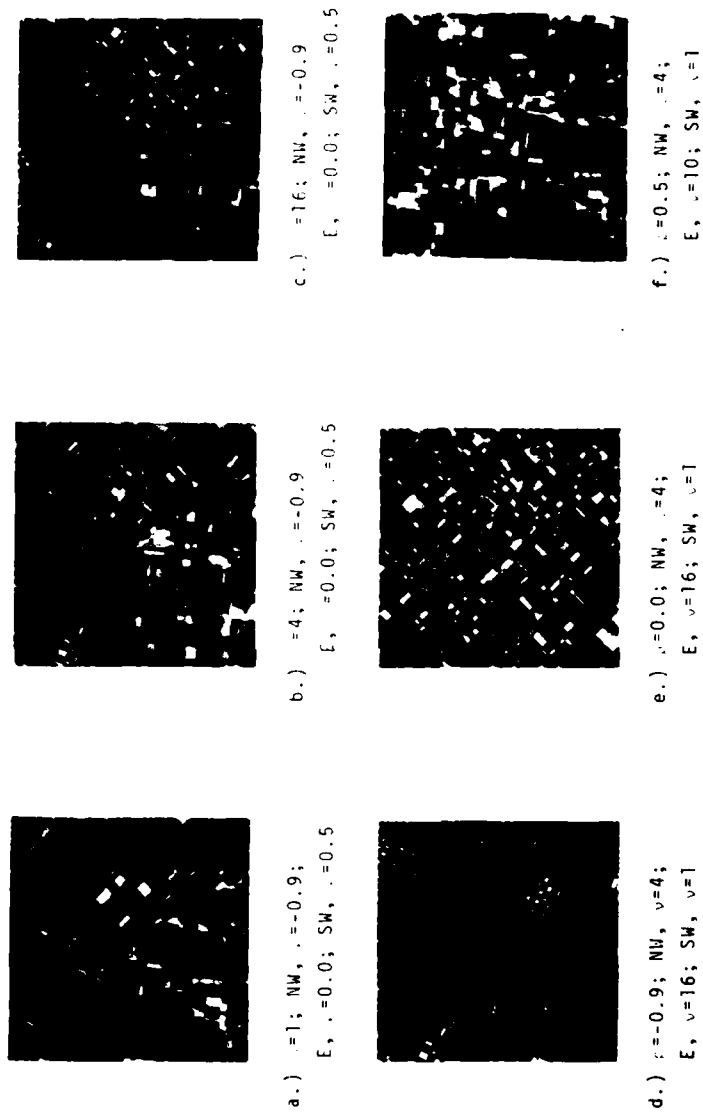


Figure 14
Typical 2-D Random Field Models of Texture;
Rectangular Partition Process with $\lambda=0.16$
and Various Values of ρ and ν

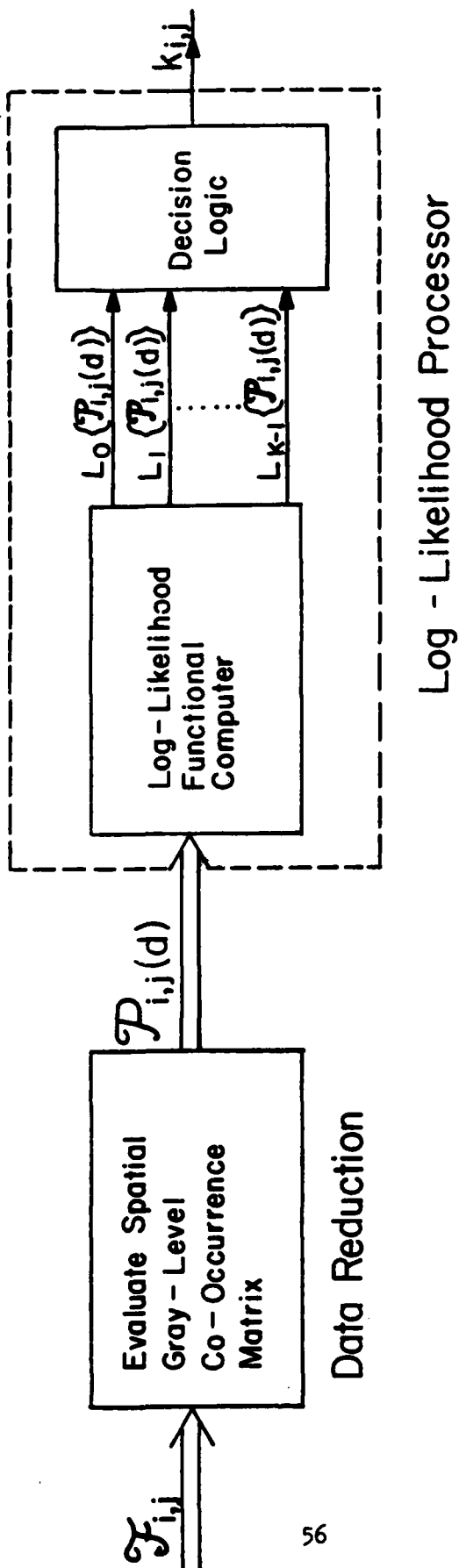
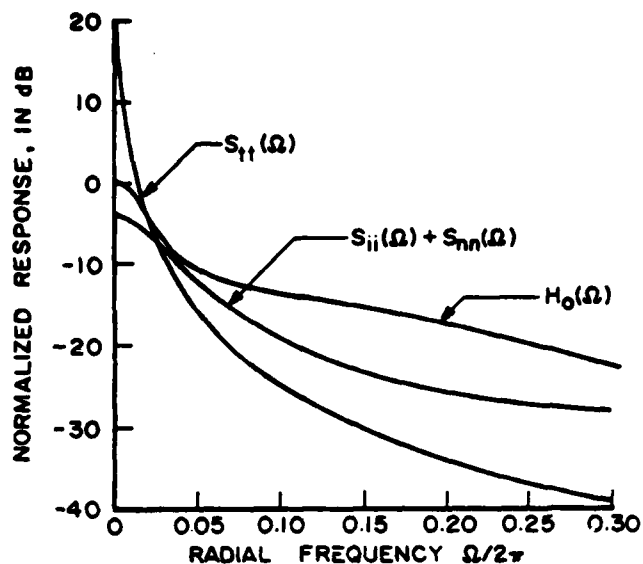
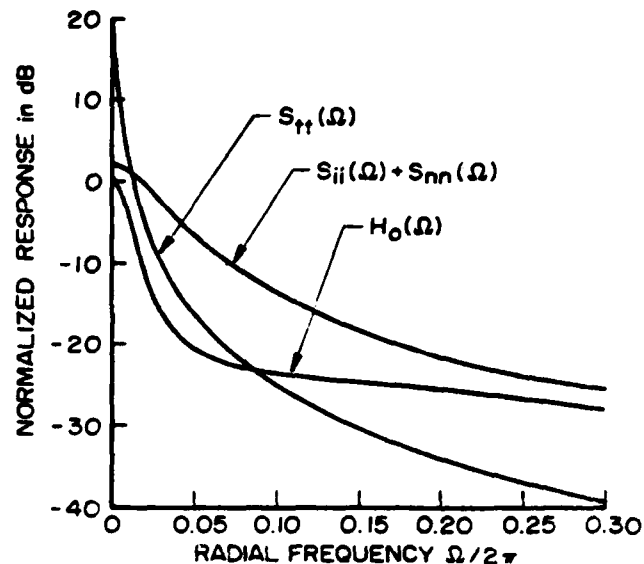


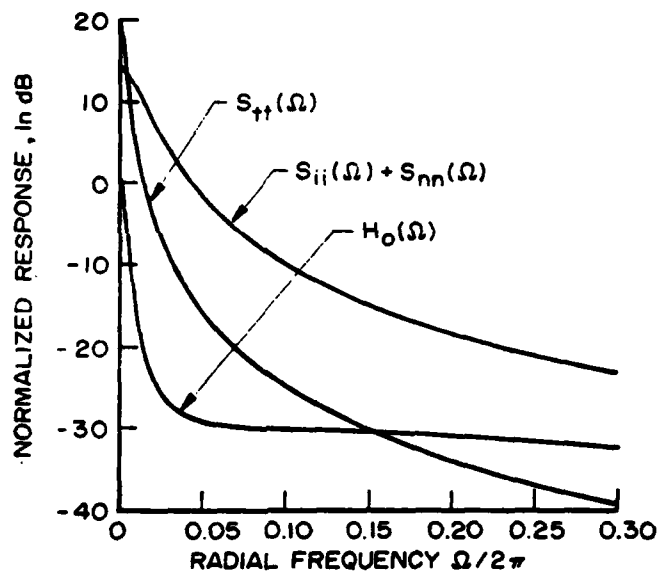
Figure 15
Log-Likelihood Texture Discriminator Based Upon
Spatial Gray-Level Co-Occurrences



a.) Weak Interference Model



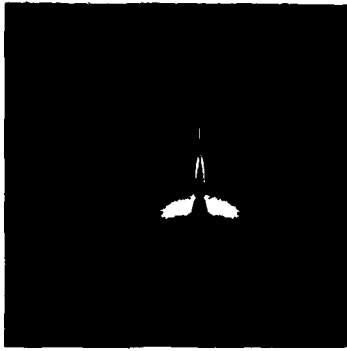
b.) Moderate Interference Model



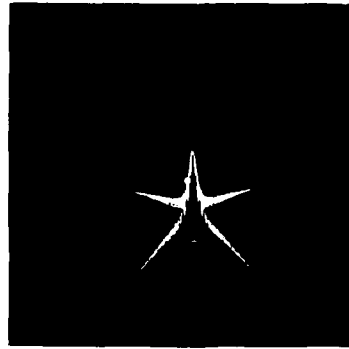
c.) Strong Interference Model

Figure 17

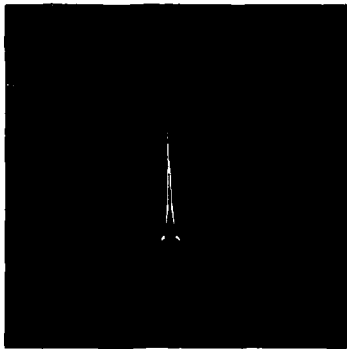
Illustration of Typical Power Spectral Densities
And Associated Wiener Filter Response



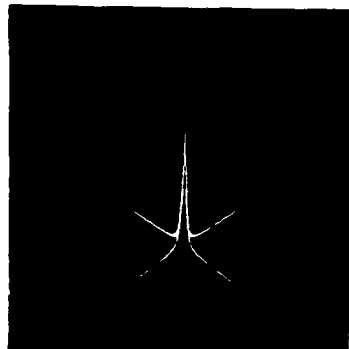
a.) Desired Response for
Weak Interference



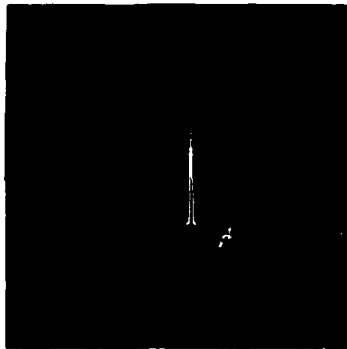
b.) Actual Response for
Weak Interference



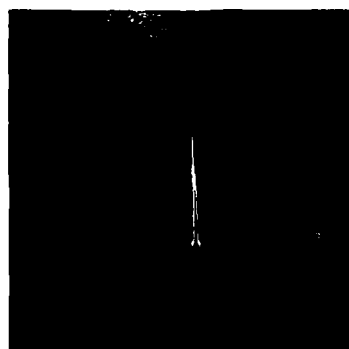
c.) Desired Response for
Moderate Interference



d.) Actual Response for
Moderate Interference



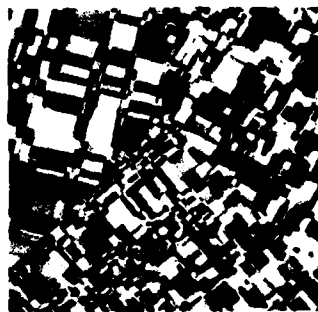
e.) Desired Response for
Strong Interference



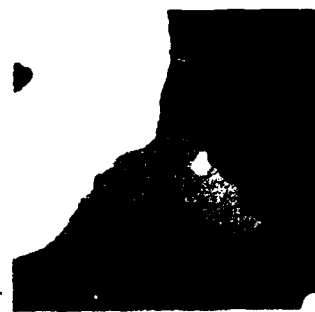
f.) Actual Response for
Strong Interference

Figure 18

Frequency Responses of Desired and Actual Filters



a.) Original ; NW , $\rho=0.0$,
 $\lambda=0.16$; NE , $\rho=0.5$,
 $\lambda=0.32$; S , $\rho=0.0$, $\lambda=$
 0.32



b.) Log - Likelihood Discriminator



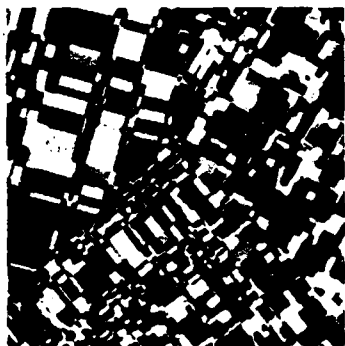
c.) Correlation Discriminator



d.) Correlation / Edge Discriminator

Figure 19

Illustration of Texture Discrimination Results



a.) Original



b.) Weak Interference



c.) Moderate Interference



d.) Strong Interference

Figure 20
Performance of Log-Likelihood Texture Discriminator
for Various Assumed Interference Levels